A METHOD OF DECOUPLING OF RADIO FREQUENCY COILS IN MAGNETIC RESONANCE IMAGING: APPLICATION TO MRI WITH ULTRA SHORT ECHO TIME AND CONCURRENT EXCITATION AND ACQUISITION

A THESIS

SUBMITTED TO THE DEPARTMENT OF ELECTRICAL AND

ELECTRONICS ENGINEERING

AND THE GRADUATE SCHOOL OF ENGINEERING AND SCIENCE

OF BILKENT UNIVERSITY

IN PARTIAL FULFILLMENT OF THE REQUIREMENTS

FOR THE DEGREE OF

MASTER OF SCIENCE

By

Ali Çağlar Özen

May, 2013

I certify that I have read this thesis and that in my opinion it is fully adequate, in scope and in quality, as a thesis for the degree of Master of Science.

Prof. Dr. Ergin Atalar(Advisor)

I certify that I have read this thesis and that in my opinion it is fully adequate, in scope and in quality, as a thesis for the degree of Master of Science.

Prof. Dr. Yusuf Ziya İder

I certify that I have read this thesis and that in my opinion it is fully adequate, in scope and in quality, as a thesis for the degree of Master of Science.

Prof. Dr. Murat Eyüboğlu

Approved for the Graduate School of Engineering and Science:

Prof. Dr. Levent Onural
Director of the Graduate School

ABSTRACT

A METHOD OF DECOUPLING OF RADIO FREQUENCY COILS IN MAGNETIC RESONANCE IMAGING: APPLICATION TO MRI WITH ULTRA SHORT ECHO TIME AND CONCURRENT EXCITATION AND ACQUISITION

Ali Çağlar Özen
M.S. in Electrical and Electronics Engineering
Supervisor: Prof. Dr. Ergin Atalar
May, 2013

In this thesis, it was both experimentally and theoretically shown that decoupling of transmit and receive coils can be achieved by using a transmit array system such that individual currents induced from transmit coils will cancel each other resulting in a significantly reduced coupling. A novel method for decoupling of radio frequency (RF) coils was developed and implemented in a transmit array system with multiple transmit coil elements driven by RF current sources of different amplitude and phase. It was shown that this method for decoupling provides isolation over 70dB between transmit and receive coils. Decoupling procedure was described and its performance was analyzed in terms of obtained isolation. It was shown that MR signal can be detected during RF excitation with the achieved amount of decoupling. NMR spectroscopy and MRI with concurrent excitation and acquisition (CEA) was implemented. As an alternative to existing CEA methods, this method reduces dynamic range requirements so that CEA sequences can be applied in standard MRI scanners with minimal hardware modification. It was also demonstrated that this method can be used to implement ultra-short echo time (UTE) imaging with shorter acquisition delay. For CEA approach, acquired raw data was formulated as convolution of the free induction decay (FID) signal and the input B1 field. First proof of concept images were reconstructed from nonuniformly sampled k space data using both UTE and CEA sequences. UTE and CEA were shown to be feasible to implement using the same custom made decoupling setup in a clinical 3T MRI scanner. Significance of imaging of samples with ultra short T2* values was discussed.

Keywords: MRI, Continuous-wave NMR, CEA, UTE, transmit array, decoupling.

ÖZET

MANYETİK REZONANS GÖRÜNTÜLEMEDE RADYO FREKANS SARGILARININ İZOLASYONU İÇİN BİR YÖNTEM: EŞ ZAMANLI RF UYARIMI VE ÇOK KISA YANKI SÜRELİ MRG'YE UYGULANMASI

Ali Çağlar Özen
Elektrik ve Elektronik Mühendisliği, Yüksek Lisans
Tez Yöneticisi: Prof. Dr. Ergin Atalar
Mayıs, 2013

Bu tezde, alıcı ve verici sargılar arasındaki izolasyonun verici dizisi kullanılarak, dizi elemanlarının oluşturduğu akımlar birbirini yok edecek şekilde sürülmesiyle gerçkleştirilebileceği deneysel ve teorik olarak gösterildi. Bu izolasyon yöntemi, paralel verici dizisi kullanılarak dizi elemanlarının farklı genlik ve fazlara sahip radyo frekans (RF) akımlarıyla sürülmesiyle gerçekleştirilmiştir. Bu yöntemle alıcı ve verici sargılar arasında 70dB üzerinde izolasyon elde edilebileceği gösterildi. İzolasyon yöntemi ayrıntılı bir şekilde anlatılarak elde edilen izolasyon üzerinden performans analizi yapıldı. Elde edilen izolasyon ile MR sinyalinin RF uyarımı sırasında gözlenebileceği gösterildi. Nükleer manyetik rezonans spektroskopi ve manyetik rezonans görüntüleme eş zamanlı uyarım ve sinyal kaydı yöntemiyle gerçekleştirildi. Bu sayede dinamik erim gereksinimleri azaltılarak standart MRG cihazlarında eş zamanlı uyarım ve data alımının gerçekleştirilebileceği gösterildi. Bu izolasyon yönteminin, çok kısa yankı süreli MRG tekniklerinin uygulanmasındaki data kayıt erteleme süresinin azaltılması için de kullanılabileceği gösterildi. Eş zamanlı uyarım MRG tekniği için kaydedilen sinyal, görüntülenen nesnenin izdüşümü ile RF sinyalinin evrilmesi olarak formüle edildi. Işınsal k uzayı tarama yöntemi ile elde edilen görüntülerle, eş zamanlı uyarım ve çok kısa yankı süreli MRG tekniklerinin tasarlanan izolasyon düzeneği ile gerçekleştirilebileceği gösterildi. Çok kısa T2* süreli dokuların görüntülenmesinin önemi MRG teknikleri üzerinden tartışıldı.

Anahtar sözcükler: MRG, Sürekli-uyarım NMR, eş zamanlı uyarım ve data kaydı, çok kısa yankı süreli görüntüleme, verici dizisi, izolasyon.

Acknowledgement

Apart from my own efforts, existence of this thesis depends largely on the encouragement and guidelines of many others:
First of all, I would like to express my deep gratitude to Prof. Dr. Ergin Atalar who made this thesis, and many other valuable works, possible by providing excellent supervision and a great research opportunity being the founder and the director of the National Magnetic Resonance Research Center (UMRAM). And I would like to thank him for giving a great deal of trust in my research capabilities, encouraging me at every step and for his endless enthusiasm and patience.
I thank Prof. Dr. Yusuf Ziya İder and Prof. Dr. Murat Eyüboğlu for showing interest in my work and allocating their precious time to read and giving critical comments on this thesis.
I would also like to mention my colleagues in UMRAM and my friends Taner Demir, Volkan Açıkel, Uğur Yılmaz, Can Kerse, Emre Kopanoğlu, Esra Abacı Türk, Aydan Ercingöz, Yiğitcan Eryaman, İbrahim Mahçiçek, Yıldıray Gökhalk, Koray Ertan, Umut Gündoğdu, Cemre Arıyürek, Dr. Oktay Algın for their mental and physical supports during my graduate school adventure. Especially Burak Akın, for sitting up together almost all the summer nights studying in UMRAM.
Finally, I will always be grateful for the unconditional supports of Semra, Hidayet and my little brother Hasan. They have always been a friendly, and understanding family whatever the choices I make in life.
I am also indebted to Uğur Erdem, my lifelong mentor for even his existence makes me a stronger person.

Contents

List of Figures

Chapter 1

Introduction

Magnetic Resonance Imaging (MRI) is known as a biomedical imaging modality that allows for obtaining soft tissue contrast. The term soft tissue has a rather vague definition and it can be inferred that it excludes tissue types such as bone, cartilage, ligaments and tendons. The main reason for low signal level from such tissues is low number of free ^{1}H protons in the tissue. ^{1}H protons bounded to large molecules has much smaller coherence when exposed to B1 field which is observed as low T2* relaxation [1]. Lungs are also difficult to obtain detailed images with MRI [2] due to susceptibility differences of tissue/air interfaces in the corous tissue resulting in a short T2* value. The problem with low T2* is basically a hardware problem, where modern MRI techniques are limited with a certain time delay between excitation and acquisition which cause signal loss in case of short T2* samples [3].

There are many special techniques developed to acquire high quality images of such short T2 samples with MRI, yet there is much to to do in this field to adapt to the clinical practice. In this thesis, we propose a method which could be used for improving MRI of ultra short T2* samples with an alternative approach. An isolation method is presented and it is claimed to be useful for applications which use information about spin dynamics in presence of RF excitation field (B1) as in the continuous-wave nuclear magnetic resonance (CWNMR) methods [4] and applications of ultra short echo time (UTE) imaging [5].

Nuclear magnetic resonance (NMR) spectroscopy is a widely used measurement technique that reveals resonance information extracted by quantum mechanical interactions describing the molecular structure of a sample. It was in 1973 when this technique was first used to generate images that map some NMR properties of a sample by a spatial encoding technique called zeugmatography [6], inherited from the back projection method commonly used in computerized tomography (CT). It took a while until the term magnetic resonance imaging (MRI) become a common use. However, apart from imaging, NMR field experienced another significant change which is related to data acquisition method. In modern applications of MRI, pulsed NMR techniques have been used since late 1970s. Whereas, the first NMR images published in a paper of P. C. Lauterbur measured the absorption of continuous-wave (CW) RF energy by the test sample as projections along specified directions using concurrent excitation and acquisition (CEA) approach [6].

In the late 1970s pulse NMR imaging techniques adopting time interleaved separation of excitation and acquisition are proposed and became more popular with the increase in the computational speed of the digital computers and the invention of fast Fourier transform algorithms. Since then, research effort is mostly focused on pulse NMR where RF is applied in short time intervals with high power instead of CW excitation with peak RF power on the order of a few hundred milliwatts. The main reasons for such a transition are that CWNMR fails to reach the signal to noise ratio levels of pulsed NMR measurements due to inherent nonlinearities of the spin systems and distortions caused by rapid frequency sweep [7]. There were efforts to improve alternative CWNMR techniques such as rapid scan correlation spectroscopy technique where undistorted high-resolution NMR spectrum is obtained from a rapidly swept RF by cross correlation with the spin response [8]. CWNMR techniques have been extensively used in NMR of solid materials with ultra short T2 values where CWNMR is able to obtain all the signal with no acquisition delay even from samples with short coherence times [9]. However, after invention of magic angle spinning method which is based on a pulse NMR approach, it has been more popular in solid state NMR. Spinning of the sample at an angular rotation rate corresponding to 'the magic angle' with respect to the direction of the magnetic field during data acquisition makes

normally broad bands of the solids narrower. Hence, resolution of the spectrum of the solid material increases [10, 11].

Although it is an old and outmoded technique, CWNMR still remains an open research area and has advantages over pulse NMR methods such as broadening the signal bandwidth and absence of a coil ring down time due to concurrent excitation and acquisition strategy. Therefore, even the structures with short coherence time could be observed without loss of information. Another significant advantage is that peak RF power is reduced into hundreds of milliwatts range in CEA approach. Although, CEA methods have been applied to industrial products and solid state materials, it has its applications in vivo where UTE and SWIFT [12] (Sweep Imaging with Fourier Transform) has their limitations such as tightly bounded water in bone minerals that is not visible using pulse NMR approaches. It is possible to investigate new contrast mechanisms and novel sequences if research effort focuses on CEA.

For in vivo applications of MRI there are methods developed with pulse NMR approach specifically for imaging tissues with ultra short T2* such as bones, tendons and cartilage [13]. Most common and popular of such methods include UTE and recently, SWIFT. UTE sequences minimize the duration between the RF pulse and the time to start data acquisition which is limited by the time needed for the energy stored in RF coils to ring down, transmit/receive switching time, and preparation time for the filters in the receive path. Duration of the RF pulse is also minimized which is of minimum 70μs for excitations of small flip angle [14]. In SWIFT, frequency modulated RF pulses are divided into segments of excitation and acquisition pairs of very short durations allowing larger flip angles for limited RF amplitude. However, lower SNR efficiency compared to UTE due to gapping and longer scan times are major drawbacks of the SWIFT method [15]. Recent studies endeavored to demonstrate the advantages and clinical applications of CW approach where MRI signal is acquired in virtually simultaneous with frequency modulated B1 excitation in SWIFT [16–21]. More recent studies demonstrated the feasibility of replacing gapped SWIFT with true CEA schemes [22]. Methods proposed for true concurrent excitation and acquisition include sideband excitation and hybrid coupler isolation. Sideband excitation

technique uses off-resonant excitation on the order of a few megahertz and filtering in time domain provides the necessary decoupling [23]. However, off resonant excitation increases RF power requirements to achieve a flip angle comparable with resonant excitation. In addition, the spins of a sample will experience Bloch-Siegert shift during off-resonant excitation. Besides, hardware to implement sideband excitation could be complex and expensive. In continuous SWIFT with hybrid coupler, decoupling enough to achieve the dynamic range is achieved by using a hybrid coupler system connected to RF coils. In this system, there is a phase difference of 180^o between the RF input port and the output port which is the input to the receiver circuitry of high dynamic range. The hybrid coupler, basically subtracts the acquired signal which is additive combination of MR signal and RF excitation from the input RF excitation signal. Due to non-idealities in the coupler circuit and frequency dependence of the performance of the coupler, RF excitation signal leaks through the receiver. Then the MR signal is extracted from the acquired data which is modeled as an additive combination of RF induced voltage and cross-correlation of the input B1 field and the FID. The needs for high dynamic range receiver electronics and extremely accurate tuning of isolator which is sensitive to the changes in coil impedance which present a difficulty for in vivo applications, along with the received signal being highly contaminated by the B1 induced imperfections are major drawbacks of the continuous SWIFT method with hybrid coupler isolation [24].

In production of this thesis, concurrent excitation and acquisition (CEA) is implemented by use of a novel method we have developed for decoupling of transmit and receive coils. This method of decoupling provides isolation over 70dB between B1 induced voltage signal on the receive coil and MR signal. This method is based on cancellation of B1 induced currents on the receive coil with appropriate adjustment of amplitudes and phases of transmit coil array inputs. Magnetic field decoupling is achieved by adjusting amplitudes and phases of the currents that drive the transmit coils. This approach is advantageous over other methods in the sense of providing higher on resonant isolation, flexibility of applied RF waveforms, and reduced dynamic range requirements. Use of transmit arrays to cancel B1 induced currents stands for an alternative decoupling method. It can

also be applied as an additional procedure to provide extra decoupling which increases MRI signal level proportionally, by reducing B1 induced voltage signal in CEA experiments [25].

The decoupling setup, we have designed, has the advantage of flexibility in data acquisition methods. The same setup and the system can also be used for pulse NMR sequences such as UTE. Using this method, acquisition delay in UTE can be reduced and CEA can be implemented in standard MRI scanners with minimal hardware modification [26]. This method makes on resonant RF excitation and concurrent reception of MRI signal possible even with standard MRI scanners without a need for increase in the dynamic range of the receiver circuitry. Reduction of B1 induced voltages on receive coil by decoupling can be useful for decreasing the ring down time which might be useful for UTE experiments. This work is partially presented in ISMRM and TMRD annual meetings as well as in CIMST summer school [25–29].

In Chapter 2, decoupling procedure is described and its performance is analyzed in terms of obtained isolation for a CEA setup composing of two transmit and a receive coil. Acquired raw data is described in terms of B1 induced voltage, response of the spins, and noise induced by transmit circuits and thermal sources. MR signal is formulated as convolution of FID and the input B1 which is a chirp signal. In Chapter 3, first proof-of-concept 2D images are reconstructed from nonuniformly sampled k space data obtained with radial inside out trajectory for both UTE and CEA. Rubbers are used in the experiments as short T2* samples. In addition, spectrum of ethanol is obtained by CEA. In Chapter 4, our decoupling method is evaluated and further improvements as well as future clinical applications are discussed. Finally, in Chapter 5, outcomes of this study are briefly recited.

Chapter 2

Material and Methods

2.1 Decoupling of RF Coils

In this section, the idea of decoupling is explained and details of implementation of this method in Siemens (Erlangen, Germany) Magnetom 3T Tx Array system are shown. Transmit RF pulse applied from a set of transmitting RF coils induce a current in the receive coil which is observed at the output of the receive coil as B1 induced voltage. Using another set of transmit coils which are called as decoupling coils driven by a certain phase, amplitude and frequency modulation characteristics such as to cancel B1 induced current generated by the set of transmitting coils. The idea of decoupling is first presented in [25].

In a concurrent excitation and acquisition experiment, acquired signal can be considered in four parts: B1 induced voltage, MR signal induced from change of total magnetization of the excited spins, transmit noise induced voltage, and the thermal noise. The signal is analyzed in terms of the weightings of its components which are B1 induced voltage, spin magnetization induced signal, and noise. MRI signal is too weak compared to RF signal. Receive circuits are designed to detect MRI signal which is on the order of tens of micro volts and the receiver system dynamic range is much lower than the B1 induced voltage level which is on the

order of volts. There is a difference roughly about 120 dB between the B1 induced voltage and the magnetization induced signal level in a typical pulse NMR experiment. This gives us a hint about the required isolation between receive and transmit coils. Initial requirement is to reduce B1 induced voltage down the receiver dynamic range. With increasing reduction in B1 induced voltage, magnetization induced signal is better quanitized which is significant for obtaining information from the spins. Therefore, decoupling enough to reduce B1 induced voltage down to the noise level is needed to acquire MRI signal directly during RF excitation with a reasonable signal to noise ratio. However, because of the imperfections of the system in use, we are not able to achieve an isolation level that would make a direct detection possible. Therefore, we need to insert a B1 induced voltage leakage in the formulation of the acquired raw data. Before reconstruction, background signal due to B1 induced RF leakage is needed to be eliminated by appropriate subtraction methods.

Decoupling procedure helps reduce B1 induced voltage. For a transmit array system with N elements some of which are used as transmitting coils and some are used as decoupling coils, we can express the decoupling task in terms of individual B1 induced currents as in Equation 2.1.

$$I = \sum_{n=1}^{N} a_n I_n = 0 \tag{2.1}$$

where I is the total current induced in a receiver coil due to transmitting coils, while I_n and a_n are B1 induced current and arbitrary complex coupling coefficient for n^{th} transmit coil. The simplest version of the described decoupling system can be implemented by two transmit coils one of which is used as the transmitting coil while the other one is the decoupling coil, and a third coil as the receive coil. An individual transmit coil, driven by an RF current I_1, induces a certain amount of current $a_1 I_1$ on the receive coil, where a_1 is a position dependent complex coupling coefficient. A second transmit coil, driven by I_2, induces $a_2 I_2$ in the receive coil. Amplitude and phase of the second transmit coil is adjusted such that $a_1 I_1 + a_2 I_2 = 0$, meaning that the total induced current in the receive coil is zero. One can solve for position dependent magnetic field component by B1 mapping of each element of the transmit array, but for our problem it is enough to know voltages induced by transmit coils individually and in total to solve Equation 2.2

for individual amplitude and phase values of transmit channels. Using individual B1 induced voltages V_1 and V_2, amplitude scale c is determined such as to set V_1 ans cV_2 equal. Using the B1 induced voltage measurement when both channels transmit, relative phase value that will provide zero total B1 induced voltage is calculted.

$$V_1 + cV_2 e^{j\theta} = 0 \tag{2.2}$$

Additional decoupling is obtained by adjusting a transmit coil and a receive coil orthogonal to each other. Such a geometrical decoupling is realized simply by rotating the receive coil with respect to the transmitting coil to reduce the RF signal coupled on the receive coil as shown in Figure 2.1. By setting the

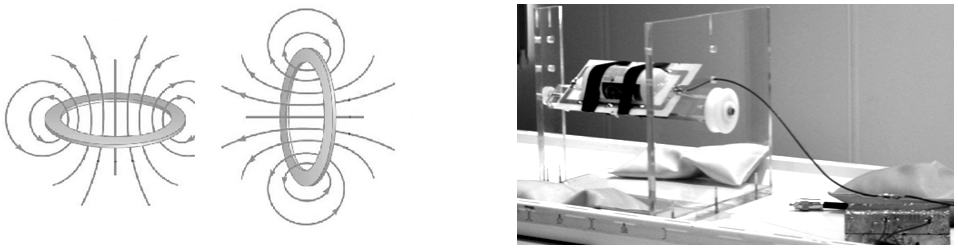

(a) Magnetic field lines (b) Rx coil rotation setup

Figure 2.1: Visual presentation of magnetic field lines for geometrical decoupling of two coils and the rotation setup we have built to implement such an orthogonal placement by rotating receive coil around the one of the transmit array coils conveniently with fine precision.

coil planes orthogonal the magnetic flux in the receiver coil would be zero in ideal case of planar coils with homogenous field distributions. In practice, field polarizations are not ideally linear but slightly elliptical which puts a limitation on the maximum achievable decoupling by geometrical means. Remaining B1 induced current due to the orthogonal transmit coil i.e. Tx coil-1 is cancelled by applying a weaker B1 from the second transmit coil with an input power accounting for the reduction achieved by geometrical decoupling and appropriate phase value. Since the B1 induced current on the receive coil due to Tx coil-1 will be reduced by geometrical decoupling, Tx coil-2 should be driven at an input power level that is lower by the geometrical decoupling amount. As a result of such an RF power level difference between the Tx coils, excitation of the spins will

be determined by the B1 field generated by Tx coil-1. Graphical representation of the decoupling procedure is shown in Figure 2.2. Apart from reduction of B1 induced currents, geometrical decoupling by orthogonal placement reduces transmit noise coupled in the Rx coil as well. Since the decoupling operation

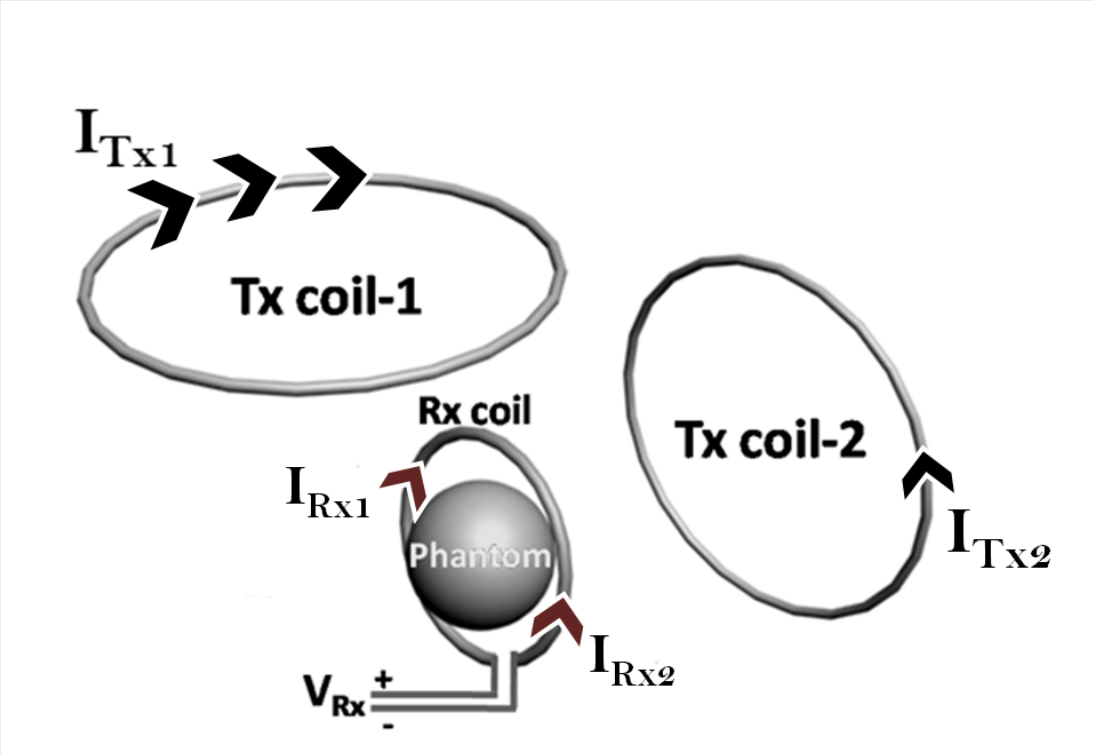

Figure 2.2: Visualization of decoupling process. First, Tx coil-1 and receive coil are placed orthogonally which reduces the B1 induced current on the receive coil as well as the transmit noise coupled current. Tx coil-1 is driven by a current I_{Tx1} inducing I_{Rx1} on the receive coil. Amplitude and phase of Tx coil-2 is adjusted such that I_{Rx2} cancels I_{Rx1} out which reduces the total B1 induced voltage V_{Rx} by a significant amount. Since I_{Tx1} is greater than I_{Tx2} by the amount of the geometrical decoupling, the spins of the sample excited mostly due to magnetic field produced by Tx coil-1.

does not change the magnetic field sensitivity of the transmit coil array, the spins of the sample still get excited due to transmit RF field resulting in an MRI signal which could be detected by the receive coil during RF excitation. Instead of coil rotation setup, fixed coil setups are more useful in the experiments. Building coils onto a hydrogen-free glass plates would be useful in MRI of samples with ultra short T2*, in terms of eliminating the background signals from polymers

which have also very short T2* values. Such a coil setup and the schematic for the whole system is shown in Figure 2.3. Siemens Magnetom 3T clinical scanner with

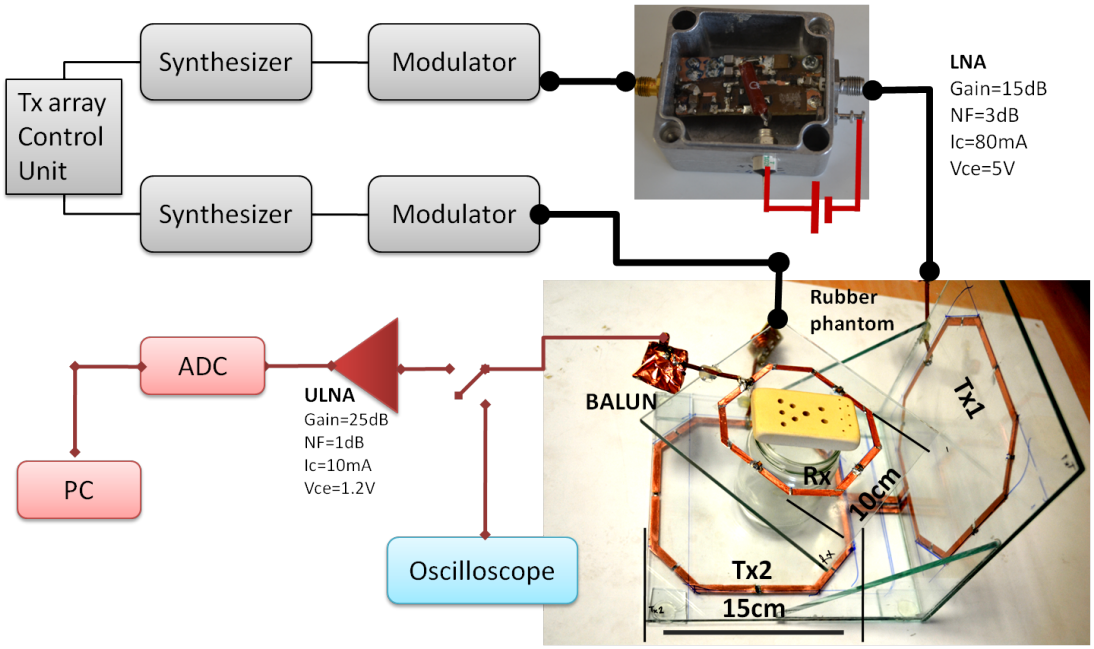

Figure 2.3: Schematic for the system setup. Transmit Array control unit controls the amplitude and phase as well as the envelopes of the RF waveforms via modulator. One of the outputs of the modulators are amplified by an LNA while the other one is attenuated by an RF attenuator in order to make B1 induced amplitudes of two transmit coils comparable to each other. Oscilloscope is used to check voltage levels at the modulator outputs and at the receive coil output real time. Once the signal voltage level at the receive coil output reduced to a value that would not saturate the receiver circuitry of the scanner, we connect our receive coil to the scanner via an ultra low noise amplifier.

8 channel transmit array system is used in the experiments. Regular RF power amplifiers (RFPA) of 70dB gain were replaced by 100mW low noise amplifiers (LNA) of 20dB gain and 2dB noise figure for CEA experiments. Design and s parameters with the noise figure and stability factor plots of the 100mW amplifier are shown in Figure 2.4. For UTE experiments RFPAs are included in the system in order to apply RF input power enough to excite the spins of the sample. The reason for replacement of system RFPAs by a ultra low noise amplifier is due to high noise contribution of regular RFPAs, giving rise to a voltage fluctuation of $400\pm100mV_{pp}$ which makes it impossible to isolate MR signal from the B1 induced voltage signal. These fluctuations are observed when the RFPAs are driven by

zero input power. The resulting oscilloscope measurements are shown in Figure 2.5 for various zoom-in levels. In addition, there are time delays between the transmit array channels due to software sychronization problems or some other inherent nonlinearities of the synthesizers. An oscilloscope screen shot is shown in Figure 2.6, displaying the signal induced in the receive coil after decouling when two transmit coils are driven by modulator outputs via system RFPAs. //
Even with the use of an LNA at the output of the modulator transmit noise could still affect the acquired signal out of a CEA experiment. It could be significant to know the limits of the transmit noise for some applications. In case of analog signal transmission, RF sources of very low noise, mixers and amplifiers with very low noise could be helpful yet the existing noise would still be amplified by the gain of the amplifiers in the transmit pathway. In Equation 2.3 total noise output power is calculated [30] for the system shown in Figure 2.7.

$$\begin{aligned} N_i &= kT_oB \\ N_o &= F_{12}G_1G_2N_i \\ F_{12} &= F_1 + \frac{F_2 - 1}{G_1} \end{aligned} \tag{2.3}$$

where N_i and N_o are input and output noise powers, respectively. k is the Boltzmann constant, T_o is the ambient temperature in Kelvin, and B is the system bandwidth. F_n and G_n are noise figure and gain, respectively, of the component n, and F_{12} is total noise figure of the system. It is shown in Equation 2.3 that output noise is determined by the gain and noise figure of the system components, thus it is significant to use low noise figure components and low noise sources in the transmission circuits.
Another noise reduction technique would be to monitor the RF during excitation by another receive channel and acquire the transmit signal alone in order to use in signal processing as a reference line. In the experimental setup described in this work, an LNA is included and also orthogonal placement of a transmit and receive coil which is called geometrical decoupling help reduce transmit noise by the amount of the geometrical decoupling.
For the first imaging experiments transmit coils were chosen as two channels of a custom made 8 channel birdcage transmit coil of 35cm diameter with loop dimensions of 8x16cm. Receive coil was a single loop coil of 6cm diameter tuned with

three distributed capacitors, matched to 50Ω, and the loaded quality factor is measured as 130. Connections are made with 50Ω coaxial cables. The coil setup is shown in Figure 2.8. This setup is later replaced by the glass coil setup as shown in Figure 2.3. Following steps are to be followed to achieve the decoupling task by decreasing the B1 induced voltage in the receive coil:

1. Using a rotation setup and transmitting RF from the transmit channel amplified with the LNA, maximum amount of geometrical decoupling is achieved by rotating the receive coil manually in angular direction while measuring the B1 induced voltage with a digital oscilloscope (DSO6104A Agilent). It is also possible to use a fixed coil setup where Rx coil and Tx coil-1 are orthogonally placed and fixed at those positions.

2. Weaker RF was applied to the second transmit coil in order to remove the remainder of the B1 induced voltage. B1 induced voltage at the receive coil output is measured and recorded for single-channel and multi-channel transmission cases. Amplitudes are adjusted such that both channel induces the same amount of voltage in the receive coil. Using individual B1 induced voltages V_1 and V_2, amplitude scale c is determined such as to set V_1 and cV_2 equal. Using the B1 induced voltage measurement when both channels transmit, relative phase value that makes total B1 induced voltage zero is calculated by solving Equation 2.2 for θ.

3. Once the voltage induced on the receiver was reduced down the measurement level of oscilloscope ($2mV_{pp}$) the receive coil output is connected to the scanner receive circuitry via a home made ULNA. Fine tuning of decoupling was proceeded by further adjustment of amplitude and phase of transmit coils iteratively from the transmit array control CPU.

A special but common case about the decoupling is the time varying pulses. The system response to the time varying frequency must be utilized in order to determine the appropriate decoupling signal. For example, if the system has a frequency response as shown in Figure 2.9b, the decoupling pulse can be calculated with respect to the original transmit pulse and the systems frequency response

as shown in Figure 2.9d. Such an adjustment that allows for transmitting different RF pulse shapes from different transmit coils would increase the decoupling performance.

2.2 Application to UTE

The idea of using reduction of B1 induced currents in UTE sequences is first presented in the literature [26] as a potential solution to the acquisition delay problem in UTE sequences due to coil ring down time. For UTE sequence, radial inside out k space trajectory with 128 radial projections of a rubber sample onto xy plane are acquired with RF pulse duration 100us and peak voltage 30V, maximum gradient amplitude 24mT/m, and acquisition bandwidth 980Hz/pixel. In radial inside-out k space trajectory, each spoke from center of the k space to the end is the Fourier transform of the projection of the sample along the corresponding gradient direction. This approach is quite similar to the projection reconstruction methods applied in CT, yet backprojection reconstruction algorithms are not preferred in MRI since they are time consuming. Gridding the projection data onto Cartesian coordinates, and then applying inverse Fourier transformation is much more popular in MRI with non-Cartesian k space trajectories [31]. Step by step description of the gridding process is stated below.

1. k space is covered in radial inside-out trajectory where each projection is a single spoke from center to the outermost point of the k space. We first define k space as a single vector and normalize the real and imaginary parts of it to scale in [-0.5,0.5]. Normalized k space coordinates are assigned to a vector named knorm which is the first parameter of the reconstruction program and has a length of 128×128 in the first experiments and 256×768 in final experiments.

2. Raw data is averaged over all the averaging acquisitions (=10 in our experiments) and arranged in a singe vector named rmean in the order of acquired projections to match the knorm vector. rmean is the second parameter of

the reconstruction and has a length of 128×128 or 256×768 where there are 128 or 256 data points for each projection spoke, respectively; and there are 128 or 768 spokes, respectively covering a two dimensional circle.

3. Density correction function is calculated according to k space sampling properties. Samples are located along radii at multiples of $\Delta k_x = \Delta k_y = \Delta k_r$. The weighting to be applied during the gridding will be the inverse of the sample density $w(k_x, k_y) = 1/\rho(k_x, k_y)$. For N_p radial projections, sample at the center is acquired N_p times. Therefore, the weighting for the samples is $\frac{1}{N_p}$ times the area of the central disk closest to the origin. Figure 2.10 shows the geometry used in calculation of the density correction function. In Equation 2.4 formula for sample weightings is shown.

$$\begin{aligned} \omega_o &= \frac{1}{N_p}\pi\left(\frac{\Delta k_r}{2}\right)^2 \\ \omega_1 &= \frac{1}{N_p}\pi\left[\left(\frac{3\Delta k_r}{2}\right)^2 - \left(\frac{\Delta k_r}{2}\right)^2\right] \\ \omega_n &= \frac{2\pi}{N_p}(\Delta k_r)^2 n \end{aligned} \tag{2.4}$$

4. As calculated in Equation 2.4, density correction function for a projection data set is simply a ρ filter.

5. Another parameter of the reconstruction funciton is cartesian grid matrix, which is assigned a square matrix for ease of calculation. It is a 128×128 or 256×256 matrix for our case.

6. Finally, we define the interpolation kernel to be used in gridding task which assigns each cartesian grid point to its value determined by convolution of the interpolation function with nonuniformly sampled data. Keiser-Bessel function is used as the interpolation kernel as shown in Equation 2.5.

$$kerneltable = \frac{1}{W}\left[\beta\sqrt{1-(2u/W)^2}\right] \tag{2.5}$$

The function is defined over $|u| < W/2$, with parameters W being kernel width and β as a free design parameter.

7. Once we form all the parameters, we calculate the gridded data points by running the grid(rmean,knorm,dcf,gridmatrix,kerneltable) function we developed using MATLAB® (version 7.10.0, Mathworks Inc., Natick, MA). This function calculates the value of each grid point based on the result of the convolution of the raw data with the gridding kernel. Raw data is multiplied by the density correction function.

8. Output of this funciton is inverse Fourier transformed and the image is formed. In Figure 2.11 gridding operation is schematically presented.

Pulse sequence diagram is shown in Figure 2.12. In the first experiments acquired raw data is mapped onto a Cartesian grid of size 128x128 for using a zero order gridding algorithm which assigns the average value of 8 closest samples in nonuniformly sampled k space data to a point on the Cartesian grid. Inverse 2D Fourier transformation is applied afterwards. Increasing the number of projections would help increasing the field of view and eliminating aliasing artifacts of high frequncy components. In order to obtain images with better signal to noise ratio, peak RF voltage should be increased. Gridding operation can also be improved by applying higher order interpolations such as Keiser-Bessel interpolation before assigning the values for cartesian grid points as stated previously. Blurring due to fast T2* decay in the acquired raw data should be corrected before gridding operation. The basic signal formulation derived for regular MRI sequences does not account for T2* decay. However, if we include this effect in the formulation [32], it is obvious that we need to deconvolve the acquired projections with reciprocal of an exponential decay determined by T2* of the sample as shown in Equation 2.6. However, multiplication of FID with T2* decay correction function results in noise amplification at high frequency regions of the k space. Such a noise enhancement can be eliminated with an apodization correction. The effect of an apodization will be observed as a gain in signal to noise ratio compared to the case with only T2* decay correction applied. These corrections can be combined in a single function with an additional constant value that prevents loss of the low frequency information. The resulting correction function is shown

in Figure 2.13.

$$\begin{aligned} s(t) &= \int m(x) e^{-j2\pi k_x(t)x} e^{-t/T_2^*} dx \\ k_x(t) &= \gamma \int_0^t G_x(t')dt' \\ s(t)e^{t/T_2^*} &= \int m(x) e^{-j2\pi k_x(t)x} dx = M(k_x) \end{aligned} \tag{2.6}$$

where s(t) is the complex FID signal in rotating frame, G_x is the gradient along x direction, m(x) is the spin density distribution along x direction, and $M(k_x)$ is the Fourier transform of the spin density distribution which is T2* corrected FID signal. As an alternative to such a correction function with sharp transitions, a function having more smooth transitions can be more useful for certain applications. One such example is given in Equation 2.7.

$$f(t) = e^{\frac{t - \frac{t}{a}^n}{T_2^*}} \tag{2.7}$$

where a and n are free design parameters describing sharpness and cut-off of the filter depending on T2* decay. Advantages of such parametric funcitons include being suitable to be used in optimization programs and eliminating artifacts due to sharper transitions in frequency domain.

In case of imaging of a sample that is a mixture of long and short T2* values, it is possible to excite only the spins with short T2* value by off-resonant excitation. Since the spins of short T2* value have broader resonance bandwidth, excitation bandwidth can be shifted such that spins with long T2* value are not excited. Note that off resonance shift must account for the existence of spatial encoding gradients as well.

2.3 Application to CEA

The expected signal for a concurrent excitation and acquisition experiment with rectangular RF is simulated in MATLAB® as the magnitude of the transversal magnetization vector during excitation [33]. Bloch equation is solved numerically using rotation matrices and the transverse magnetization is calculated under the small-tip angle approximation [34] as shown in Figure 2.14. Simulation results

show that a decaying oscillation should be observed out of a CEA experiment, where the decay and oscillation characteristics determined by B1 field magnitude and relaxation parameters of the sample . Time constant of the decay is determined by the T2* value of the sample. Peak amplitude of the decaying oscillation depends on the B1 field magnitude. The magnetic field strength will determine the received signal magnitude. Note that in the simulation, noise sources and any other influences of experimental complications such as imperfections in decoupling are ignored.

In NMR theory spins are described as linear systems with the impulse response being the free induction decay (FID) behavior of the spins under relaxation. A CWNMR experiment is modeled as a linear system operation where the input is B1 excitation signal and the output is the convolution of the system response (FID) and the input B1 which is a chirp signal covering a certain frequency range [35]. Detailed formulation is also given in literature [8] for short T2* and small tip angle approximation in order to account for linearity condition of spins during CW excitation. Acquired raw data in a CEA experiment can be formulated as additive combination of such a convolution signal and a frequency dependent leakage component which is the remaining B1 induced voltage due to limited decoupling as shown in Equation 2.8.

$$\begin{aligned} s(t) &= FID \otimes B_1(t) + A(t) \\ s(t) &= FID \otimes B_1(t) + h(t) \otimes B_1(t) \\ B_1(t) &= e^{-j\pi f_s / t_{acq} t^2} \end{aligned} \tag{2.8}$$

In Equation 2.8, A(t) is the frequency/time dependent leakage signal due to insufficient decoupling. We can model this leakage by an experimentally determined system response h(t), which is the time dependent response of the data acquisition system against the B1 induced voltage. Since the frequency is swept linearly through time, the leakage response can also be treated in frequency domain which is an intrinsic property of the chirp signal. h(t) can be measured separately in a CWNMR experiment provided that no MR signal exists in the acquired signal. The ratio of frequency sweep range f_s and the total RF duration t_{acq} is regarded as the frequency sweep rate. In literature [36], the leakage signal for hybrid coupler systems used in classical CWNMR systems with lock-in detection is formulated

as in Equation 2.9.

$$A(w) = \frac{R_{coil}}{1 + \Delta w^2 \tau^2} + j \frac{R_{coil} \Delta w \tau}{1 + \Delta w^2 \tau^2} \tag{2.9}$$

It is reported in [24] that a second order fitting is sufficient to approximate A(w) (We use A(t) analogically to A(w) due to linear sweep of frequency over time) instead of solving equation 2.9 analytically. Another method is to measure the received signal when the receive coil is unloaded [37]. In the CEA experiments, two subsequent data are acquired, one with the regular experiment setup and the other with the sample is removed. The difference of two cases is considered to be the raw MR signal that is to be deconvolved with B1 to get FID response. The measurement data when the sample is removed is used as B1 signal. Note that the amplitude of the B1 induced leakage signal may differ for subsequent measurements due to instabilities occurring in Tx-Array control unit. Therefore, we take averages of repetitive measurements to account for a better fitting.

It should be noted that position dependence of B1 is ignored in Equation 2.8. B1 inhomogeneities were not taken into account during experiments, as well. In future studies, in order to make position dependence of B1 ineffective, adiabaticity of the applied B1 waveform should be increased since adiabatic pulses rotate the magnetization vector at constant flip angle, even when B1 is extremely inhomogeneous [38].

We drive Tx coil-1 from a Tx array modulator output via an LNA, while Tx coil-2 is driven directly from the modulator output without amplification. Orthogonal placement of Tx coil-1 and Rx coil is significant to reduce transmit noise coupled on the receive coil in CEA applications. Decoupling is done by adjusting amplitude scales and relative phases of Tx coil-1 and Tx coil-2 so that individual B1 induced currents on the Rx coil cancel each other. Tx coil-1 is driven with RF input power of 8mW and Tx coil-2 with 0.4mW. After the decoupling is achieved, B1 induced voltage is reduced to 0.5mV including the preamplifier gain of 35dB with 0.8dB noise figure. First experiments are conducted with a rectangular receive loop coil loaded with a plastic bottle of 7cm diameter and 15cm height full of tap water solution of 1gr/l saline and 1gr/l CuSO4 (ε_r=60, σ=0.2 S/m). See Apendix A for measurement of dielectric constant and conductivity values. For the recent imaging experiments a glass coil setup is used instead of the plastic

one in order to prevent background signals formed by ultra short T2* substances. Liquid samples used for loading of small loop coil are put in a cylindrical glass cup with 6cm diameter and 5cm height. 50% ethanol and water solution is the liquid sample used for spectroscopy experiment. Chirp pulses with certain frequency sweep range and pulse durations are calculated in MATLAB® and inserted in pulse sequence executive files using pulse programming environment IDEA of Siemens Medical Systems. Zero gradient case and gradients corresponding to radial k space trajectory are also programmed using IDEA as shown in the pulse sequence diagram of a single TR duration in Figure 2.15. Raw data is read and saved with a MATLAB® program and average of 10 acquisitions for each case is assigned to vector variables. Reconstruction formula is inserted in a MATLAB® function and 1-D projections are calculated along each gradient direction as well as the spectrum of the sample.

$|B1|$ value is also calculated using Bloch-Siegert shift method in order to estimate the flip angle. In B1 mapping with Bloch-Siegert shift method, an off resonant RF is applied which results in spins to experience an additional phase shift. Using the fact that the additional phase is proportional to $|B1|^2$ it is possible to get B1 map from the phase images [39]. B1 maps are generated for reference input voltage level of 20V with a Fermi pulse of 8ms duration and 4kHz off resonance from the center frequency using the Equation 2.10 after unwrapped phase maps are obtained [40]. This reference value is used to approximate the flip angle and B1 values achieved in CEA experiment by assuming that the flip angle and B1 value are linearly dependent on the input voltage level and the RF duration.

$$\phi \approx \int_0^T \frac{|\gamma B_1(t)|^2}{2\omega_{OFF}(t)} \mathrm{d}t. \tag{2.10}$$

where ϕ is the phase value and ω_{OFF} is the off resonance of the RF pulse from the center frequency. Note that this equation for $|B_1|$ is an approximation and can be corrected with a modification that includes higher order terms [41]. However, for the small flip angle values as in our case, it should be a valid approximation to use Equation **??**

Chirp RF pulse of 0.5V with 4.2ms duration and 4.2kHz sweep range is applied and acquisition is started 100μs after RF starts. Reconstruction of CEA data starts with subtracting the remaining RF leakage induced in the receive coil from

the acquired raw data. Deconvolution of the raw MR signal with the measured B1 field is done afterwards for each projection line. The rest is the same gridding approach as in the UTE reconstruction. It should be noted that no filters or any other signal processing is applied to the raw data except the RF leakage subtraction, deconvolution, and the zero-order gridding operations unless specified.

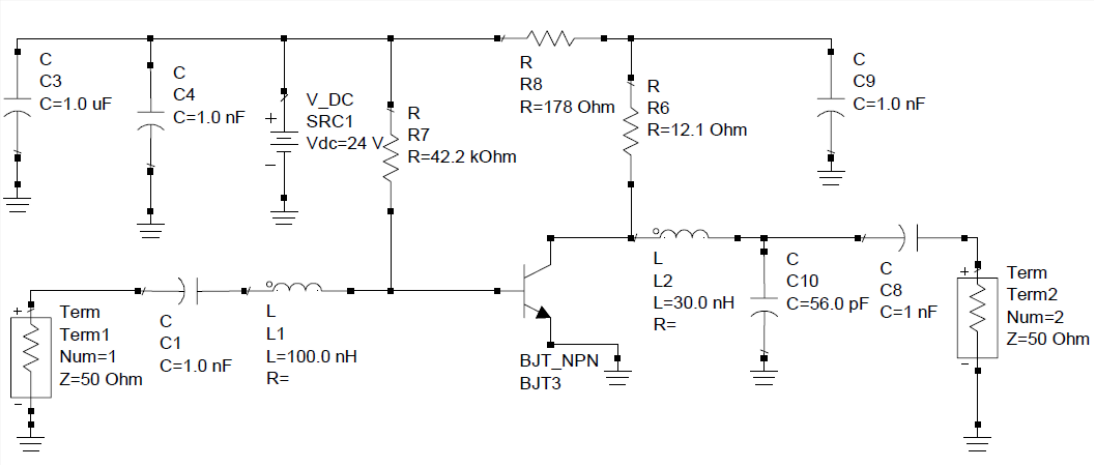

(a) Circuit diagram of the LNA

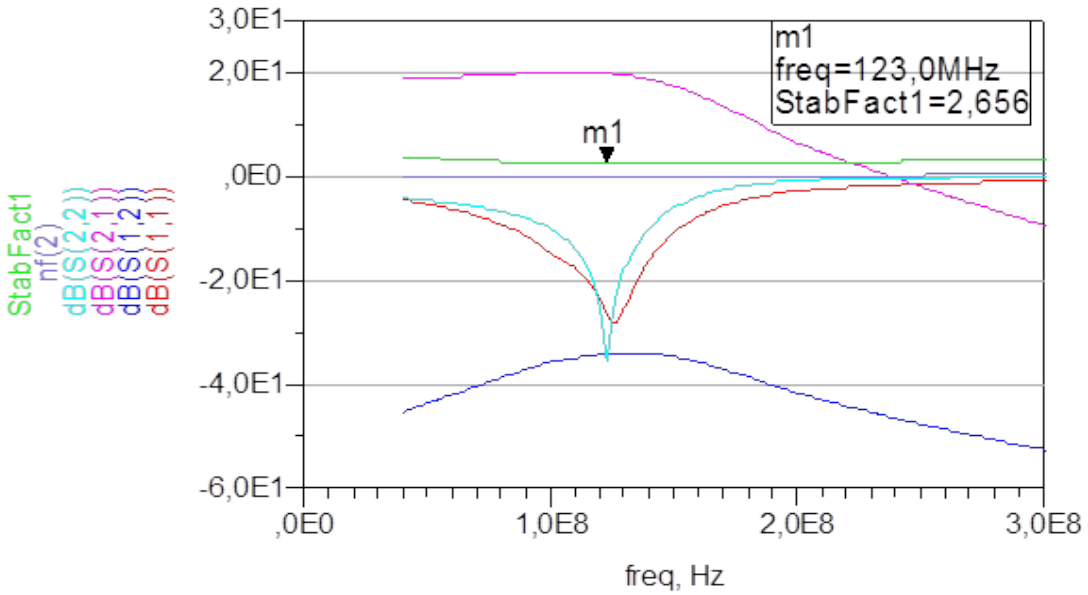

(b) S parameters, Noise figure and Stability Factor

Figure 2.4: Circuit diagram and s parameters with noise figure and stability factor of the amplifier used in the experiments. Single stage amplifier is built with a BFG135 bipolar transistor with input and output matchings are performed.

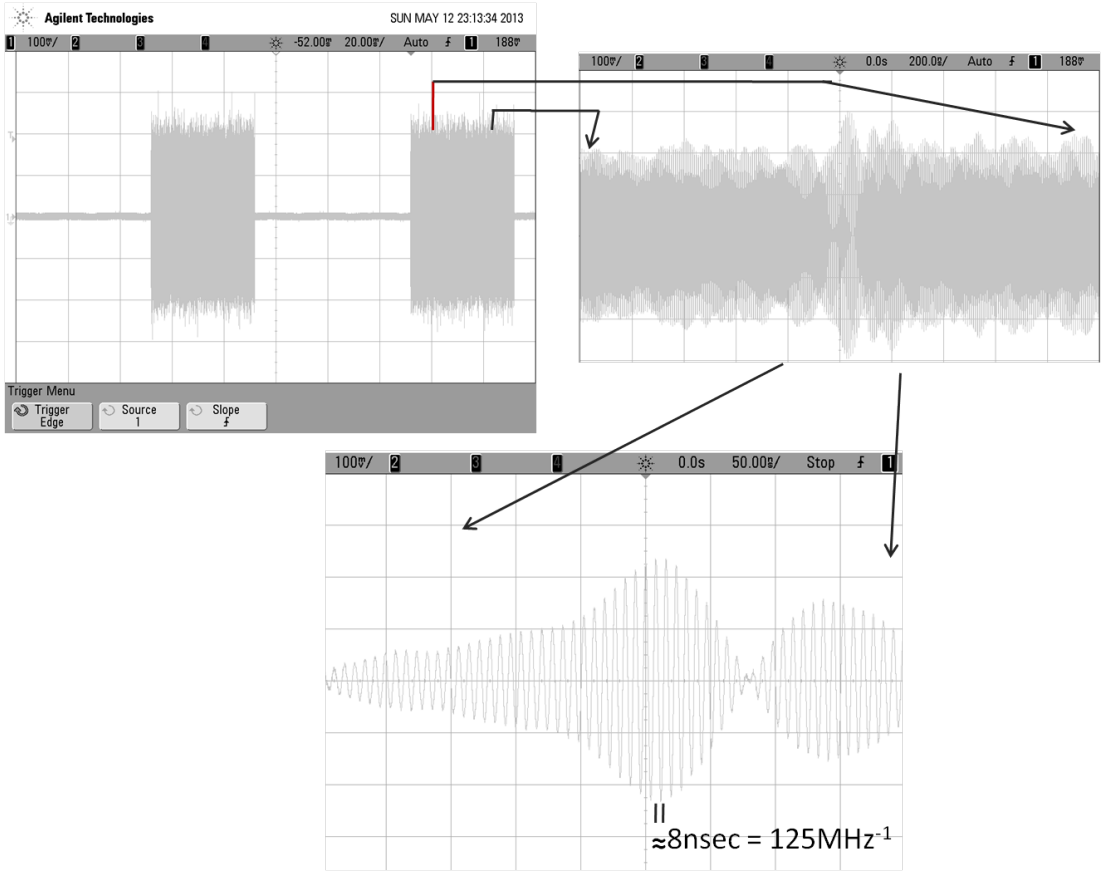

Figure 2.5: Distortions on the output waveforms of the original 4kW system RF power amplifiers measured with oscilloscope. System RFPAs are driven by input RF signal amplitude of which is set to zero from MR console. Nonlinear effects of the amplifiers are observed as $400mV_{pp}$ fluctuation signals.

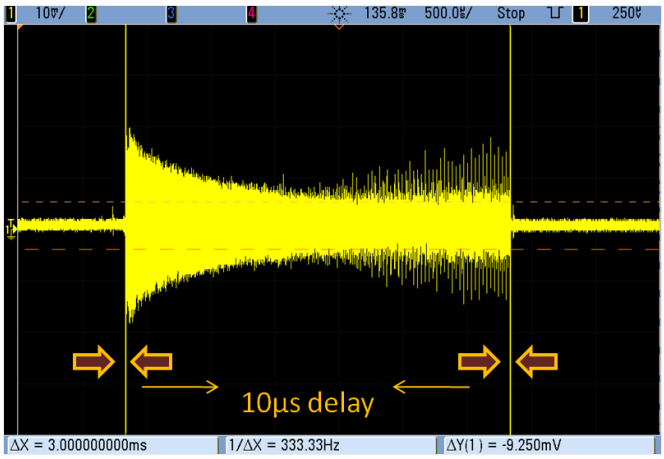

Figure 2.6: The peaks are observed at the end of signal envelope due to a delay about 10μs between transmit channels. This effect is eliminated in the CEA experiments by starting acquisition 100μs later than RF starts.

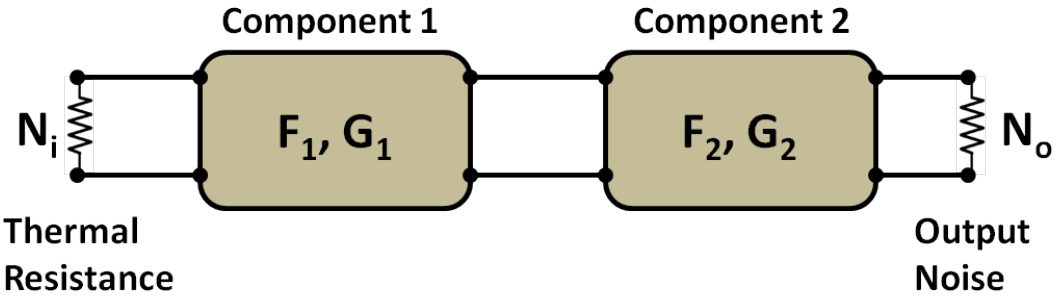

Figure 2.7: System with a thermal noise source, and two active components.

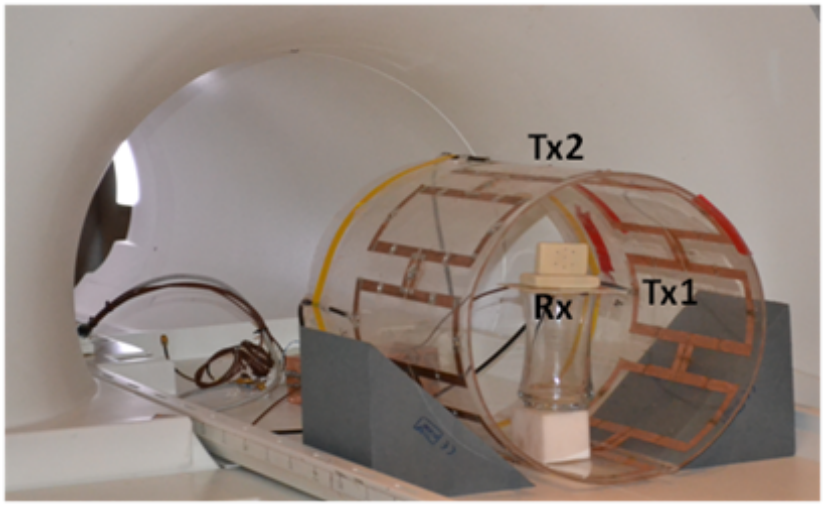

Figure 2.8: Experimental setup with a 8 channel birdcage transmit and a receive loop coil. A rubber phantom is placed on the receive coil.

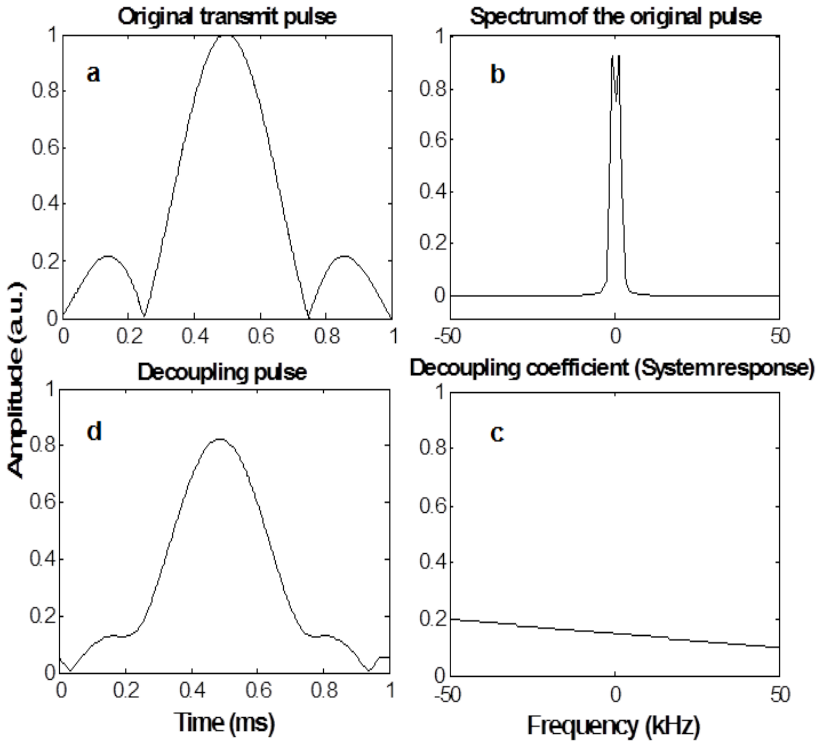

Figure 2.9: Demonstration of decoupling when B1 induced voltage signal has a time dependence. Transmit sinc pulse with a single side lobe (a). Spectrum of the sinc pulse (b). Frequency response of the decoupling system in 1024Hz range (c). Required transmit pulse for better decoupling than decoupling using the same pulse transmitted from both sources (d).

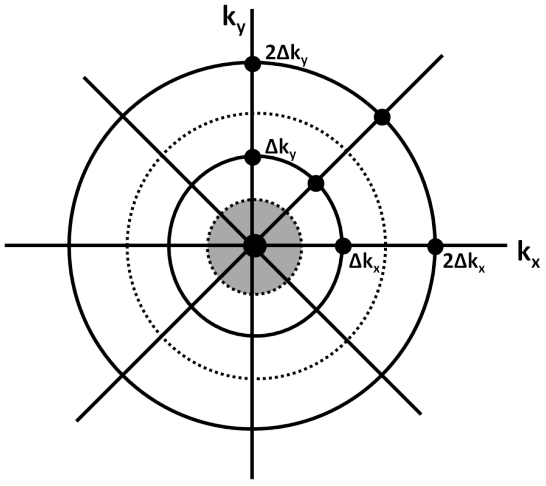

Figure 2.10: Calculation of the sampling density for a projection raw data set.

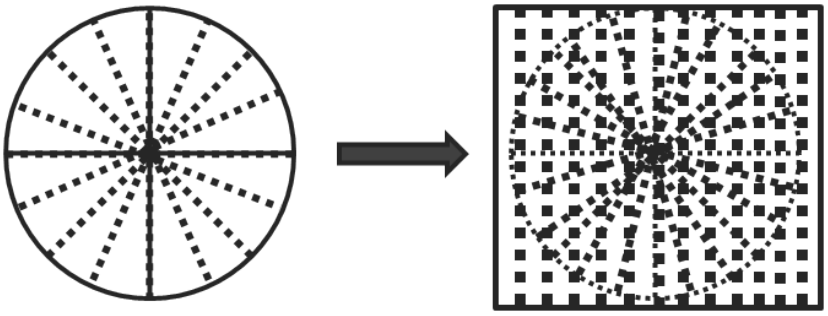

Figure 2.11: Nonuniformly sampled data is transformed into Cartesian grid points. Value of a grid point is assigned by interpolation.

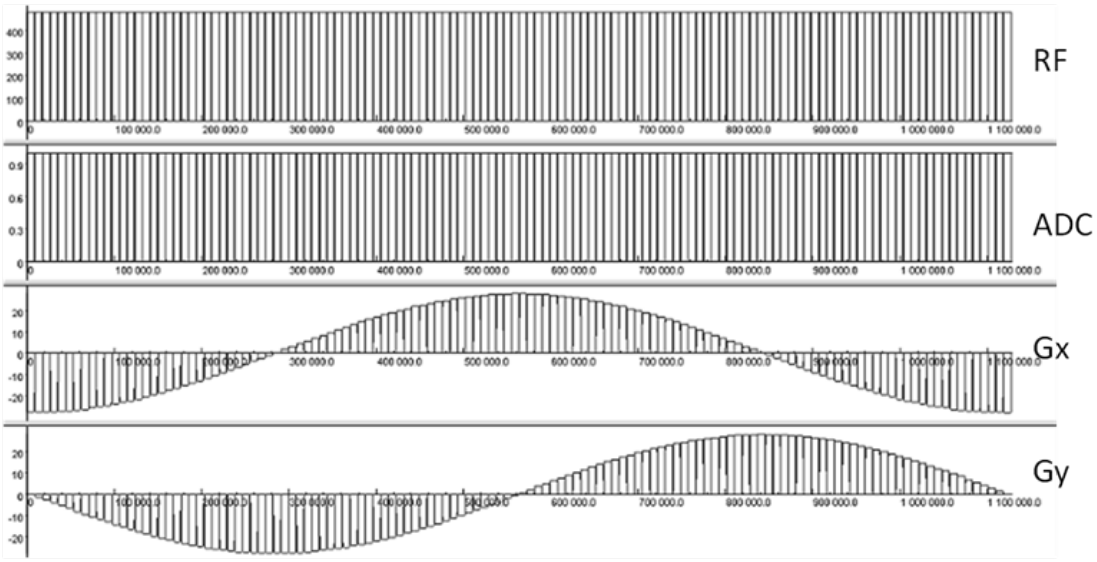

(a) UTE pulse sequence diagram for radial k space trajectory

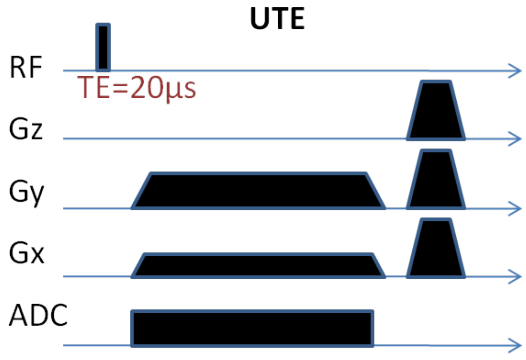

(b) Pulse sequence diagram for a single TR

Figure 2.12: Pulse sequence diagram for CEA with 128 radial projections and a single time of repetition (TR) interval.

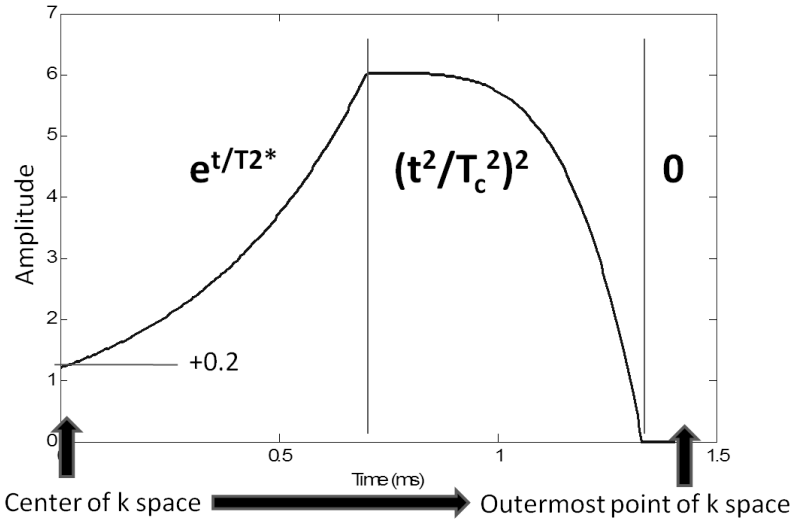

Figure 2.13: T2* correction combined with apodization correction and additional constant. The correction function was determined experimentally by trial and error method once we measure the T2* of the sample as 450μs with a UTE relaxation sequence. Each raw FID signal is multiplied with this correction function for enhancement of high frequency information.

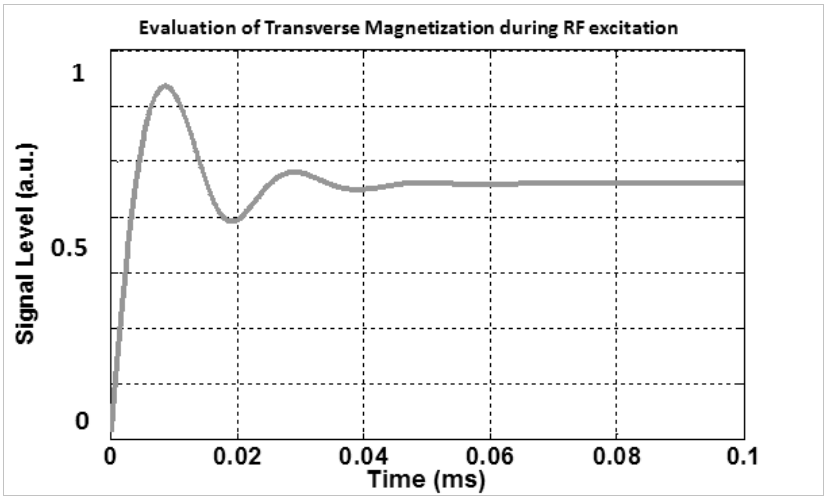

Figure 2.14: Transverse magnetization during rectangular B1 excitation calculated from Bloch equation under small tip angle assumption for a sample with T2 of 1ms.

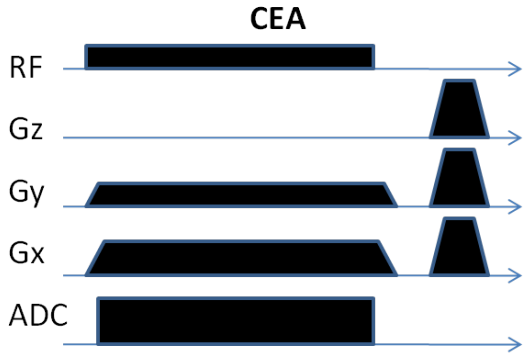

Figure 2.15: Sample pulse sequence diagram representing excitation, acquisition and encoding timings and magnitudes for a single TR interval. Gradients along with the sweep range determine the FOV and resolution. Changing the orientation of the gradients means acquiring projections along various directions.

Chapter 3

Results

3.1 Decouping of RF Coils

We achieved decoupling of 70dB which corresponds to total of 20dB geometrical decoupling and 50dB multiport decoupling. In the beginning, the receive coil loaded by a sample of copper sulfate solution is attached to the rotation setup and placed in the scanner. Then, coil plane is rotated counter clockwise with a step size of 5^o. The voltage induced in the receiver coil, which is measured $80 \pm 5mV_{pp}$ at its maximum, is recorded by the oscilloscope. The rotation step size is reduced to 0.5^o when needed in order to observe the induced voltage to be decreased. Resulting plot for geometric decoupling simulation and experimental data are shown in Figure 3.1. Geometric decoupling is done for one RF generator unit connected to one of the channels of the birdcage coil with an LNA of 20dB gain and 2dB noise figure connected at the modulator output. Then, the other channel of the modulator output of the RF generator unit is connected directly to another channel of the birdcage coil with an attenuator enough to adjust individual B1 induced voltages close to each other, in this case 6dB attenuator was used with the initial setup. For the glass coil setup, tuning of the Tx coi-2l is shifted from on resonant in order to reduce the coupling instead of using attenuators. Once a second RF generator unit is connected to the second transmit

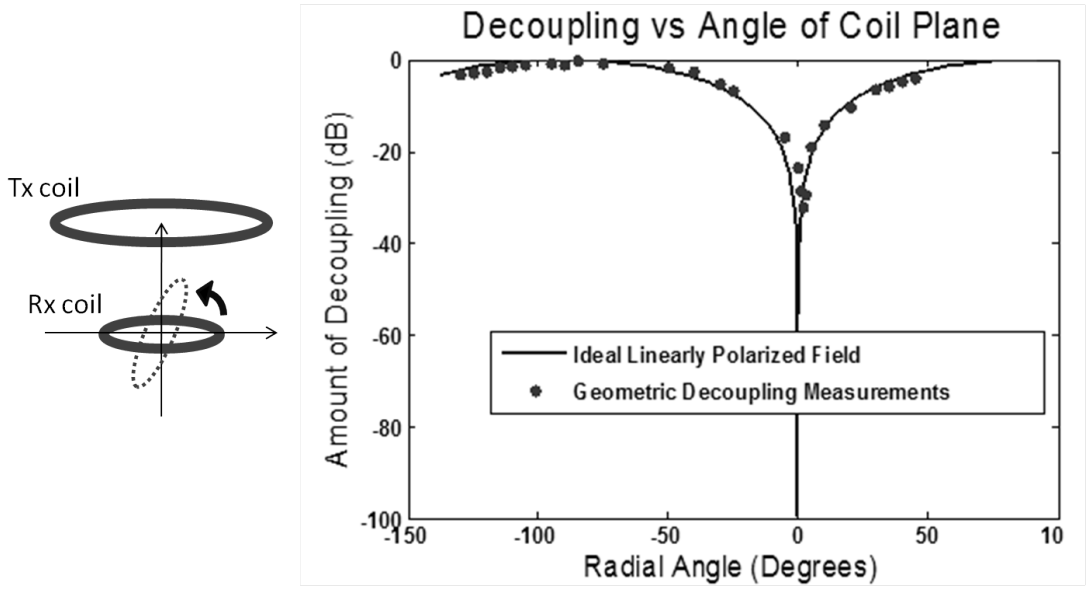

Figure 3.1: B1 induced voltage is measured for rotation of the receive coil plane with respect to one of the transmit coils covering 180^o. Ideal linearly polarized field is calculated and both normalized to 0^o to impress the effect of getting closer to ideal condition. The limitation in this task is that individual polarizations of the transmit coils are slightly elliptically polarized. One should also consider physical dimension of the coils and the distance between them because receive coil can affect the loading of transmit coil when they are placed too close to each other and their physical dimensions are similar, due to strong mutual coupling.

coil, we record the voltages induced by single channel transmissions and multi-channel transmission. Using the recorded data, the phase value that minimizes total B1 induced current is calculated. Observing the induced voltage, phase of one of the RF generator units is adjusted within possible precision via transmit array control unit. Initial voltage of $8 \pm 1mV_{pp}$ that corresponds to the voltage induced after the geometrical decoupling is reduced further to $6 \pm 4\mu V_{pp}$ with multiport decoupling after phase adjustment. Induced voltage is recorded for a range of relative phase values of the RF generator units with step size of 10^o. Step size is reduced when required. The resulting plot for achieved decoupling is shown in Figure 3.2. Orthogonal placement of transmit and receive coils helps reduce transmit noise induced voltage signal as well as the B1 induced voltage. We expected that the transmit noise induced voltage would be a dominant factor in the acquired signal. However, we observed that acquired signal voltage levels were the same for two cases: when the transmit system is driven by zero input

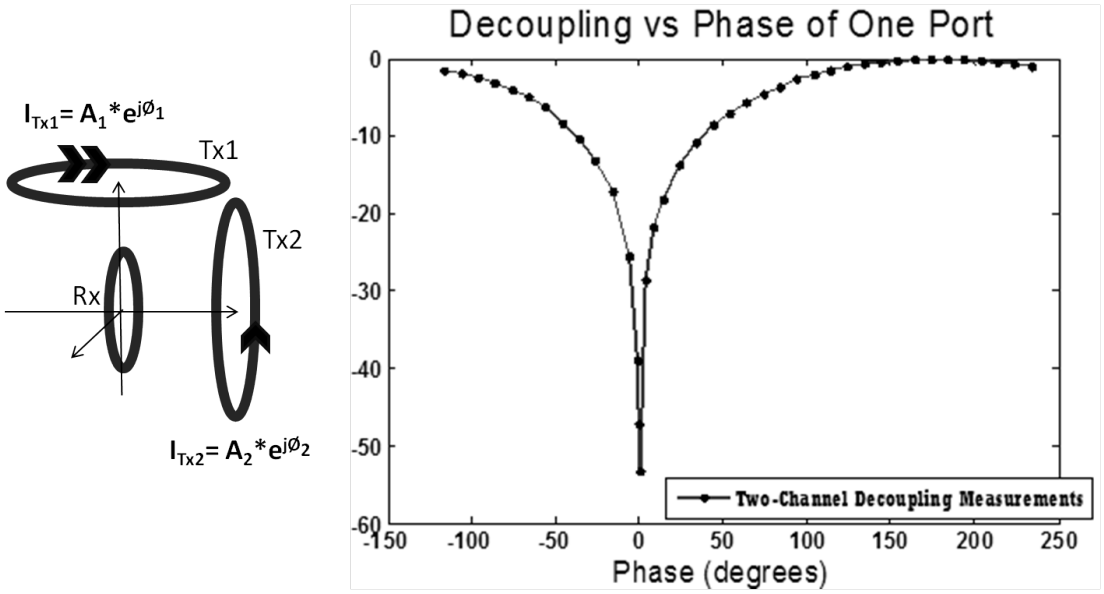

Figure 3.2: Decoupling versus Phase of an RF generator unit. Two-port decoupling is represented by changing the phase of one port in uniform steps covering 360^o. Data are normalized to 0^o. Limitations of decoupling using this procedure arises from the precision of the phase control unit. Stability of the RF generator unit is also a key factor for the achieved decoupling to be preserved during the experiment. Addition of a third coil could increase the amount of total decoupling which could be used to cancel remaining B1 current on the receive coil.

power; when the transmit system is turned off. Therefore we concluded that the transmit noise induced voltage is lower than the receive noise floor, whereas calculation of transmit noise could be needed for extreme conditions with higher transmit noise. The effect of geometrical decoupling on reduction of transmit noise is demonstrated in Figure 3.3 where B1 induced signals are shown from an experiment with multiport decoupling applied alone, and various levels of geometric decoupling applied with multiport decoupling. It is shown that increasing the amount of geometrical decoupling, noise fluctuations in the receive coil decreases. The problem with multiport decoupling is that when the transmit fields are of different sources, they have different noise characteristics and it is not possible to decouple noise with B1 induced current cancellation technique when the noise has uncorrelated sources. However, orthogonal placement simply eliminates the B1 induced current by all means whether it is noise or the signal itself. // Another experiment is conducted to demonstrate the feasibility of decoupling with

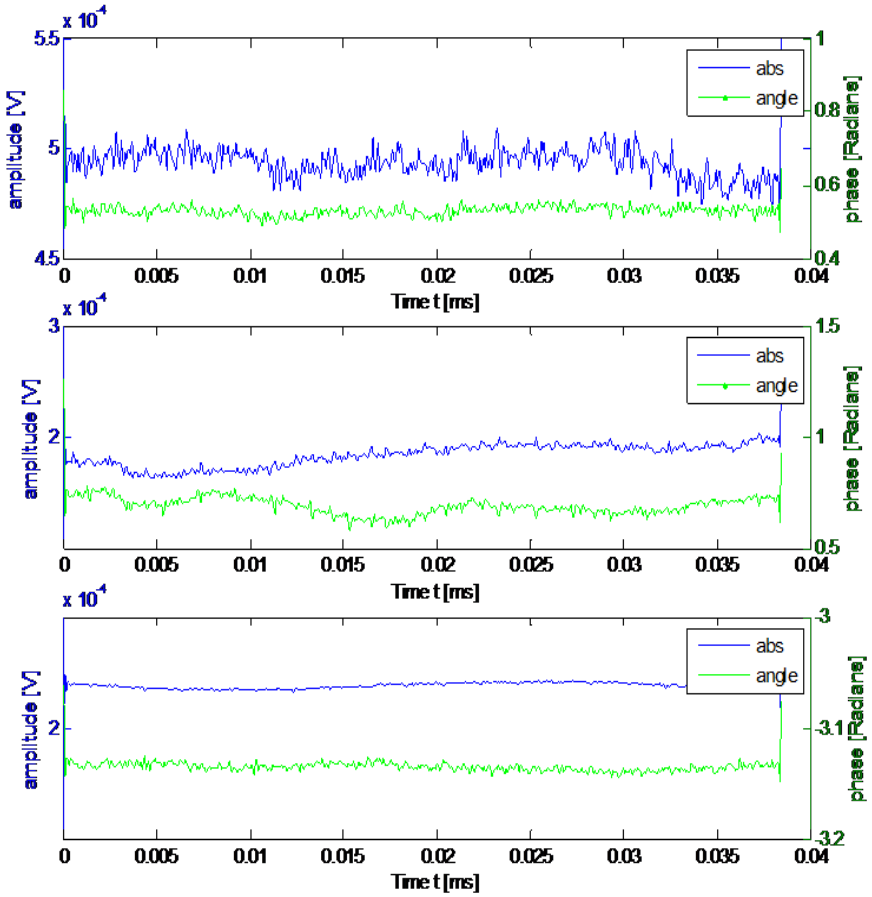

Figure 3.3: B1 induced voltage signal in the receive coil after decoupling. Multiport decoupling without geometric decoupling (a), Multiport decoupling with 10dB geometric decoupling (b), Multiport decoupling with 20dB geometric decoupling (c).

transmit RF pulses of different shapes. One such example is shown in Figure 3.4 where the system frequency response is used to obtain optimum RF waveform to be transmitted from second transmit channel for better decoupling. The resulting B1 induced voltage signals after decoupling are compared for the same RF and different RF waveorm cases in Figure 3.5. It is observed that, estimating the RF waveform to be transmitted from the decoupling coil based on the system response reduces the deviation of leakage level with respect to the frequency. The amount of achieved decoupling is also increased when two transmit coils are driven by different RF waveforms. However, the system stability prevented us from using this approach in imaging experiments. The system response shows

variability among the experiments and also it is time consuming to update the estimated RF waveform each time. Therefore, in this study we only show the feasibility of this approach in decoupling procedure which could be improved and further utilized when system stability problems are resolved by designing more reliable system components.

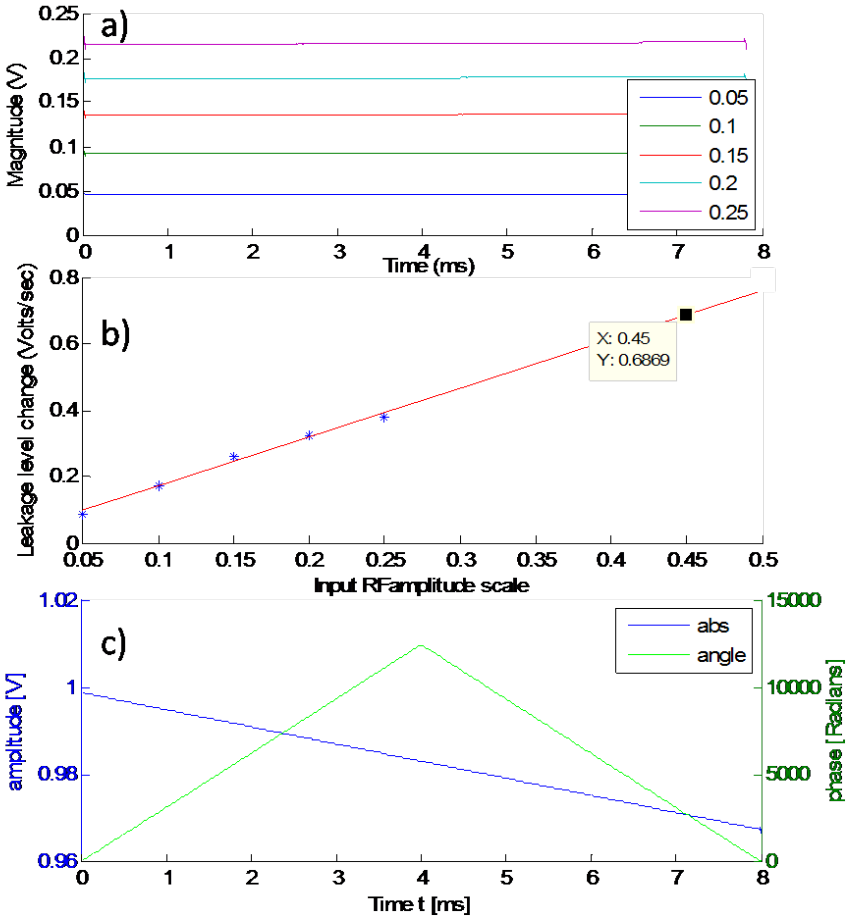

Figure 3.4: B1 induced voltage signals in the receive coil for single channel transmission with varying input levels by changing the amplitude scale of a chirp RF signal spanning -8kHz to 8kHz over 8ms from Tx array user interface (a). Estimated system response for actual input level (b). Estimated RF waveform to be transmitted from the decoupling coil i.e. Tx coil-2 (c).

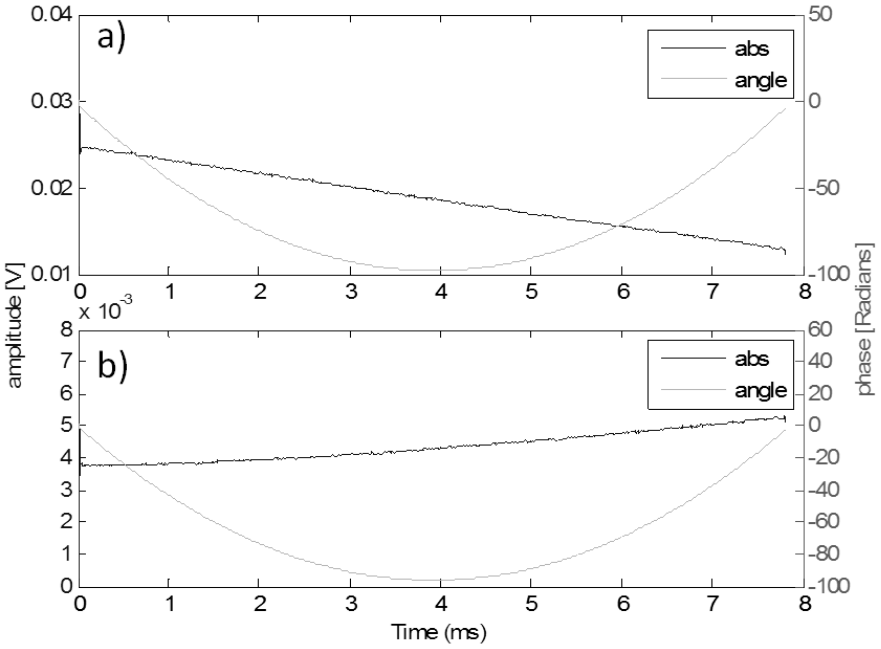

Figure 3.5: B1 induced voltage signal in the receive coil after decoupling with the same RF waveform transmitted from both transmit channels (a), and a different RF waveform transmitted from the decoupling coil as shown in Figure 3.4c (b).

3.2 Application to UTE

2D image for UTE is shown in Figure 3.6. There are artifacts based on the projection reconstruction method employed here is not being so powerful. Center of k space is missed in the UTE data which result in center brightening artifact. However, the dots and the edges as high frequency information are represented in the image clearly. It is expected that the time delay between the RF turn off and acquisition start would be decreased with increasing amount of decoupling yet this could not be demonstrated in the imaging experiments because we had to include RFPAs in our setup. RFPAs induce high levels of fluctuation signal due to blanking of the RFPAs before transmission starts and this prevents us from decreasing the acquisition delay further than 20μs. In fact, a time delay of 10μs between the transmit channels which resulted in spikes at the end of the RF pulse is observed and we had to put a 20μs time delay at the end of the RF before starting the acquisition in UTE sequence. Increasing the input RF peak voltage to 240V and the number of k space lines to 768, we observe

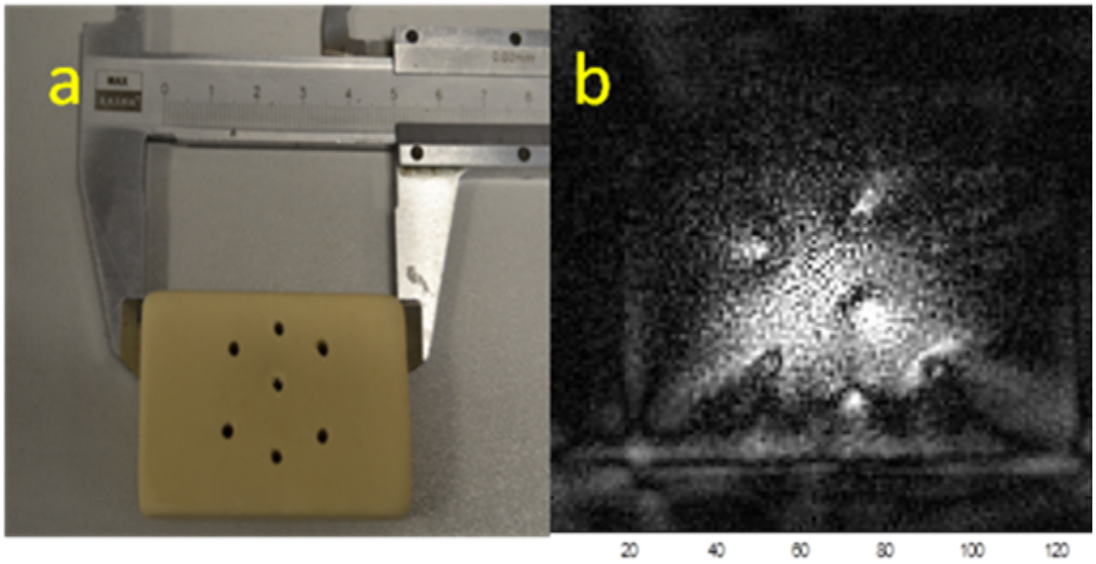

Figure 3.6: Rubber phantom with holes (a). UTE image for 128 projections and 30V peak RF input voltage (b).

in Figure 3.8a that the signal level increases, yet there are still artifacts in the image. Another improvement is the use of Kesier-Bessel interpolation and sampling density correction for gridding operation. Sampling density correction matrix is formed by calculating the sampling density along the angular direction from inside out. The samples become less dense when we move away from center. For the k space trajectory used for 768 lines with max gradient level of 14mT/m the density correction over each projection is included in the gridding process. T2* correction is also applied to the acquired data which enhances the edges of the image of the rubber as shown in Figure 3.8b. The effects of T2* correction on the FID signal and a single projection are shown in Figure 3.7. In Figure 3.9 the effect of acquisition delay on the image quality is demonstrated as well. Increasing the time between excitation and acquisition we start to lose information which becomes even more obvious for samples with short coherence time. We observe that image quality increases with increased number of projections. The effect of T2* correction is observed as sharpness in the projections which explains the reason for edge enhancement of the image. There are some other artifacts in the image that should be eliminated before advancing to a clinical application of these sequences.

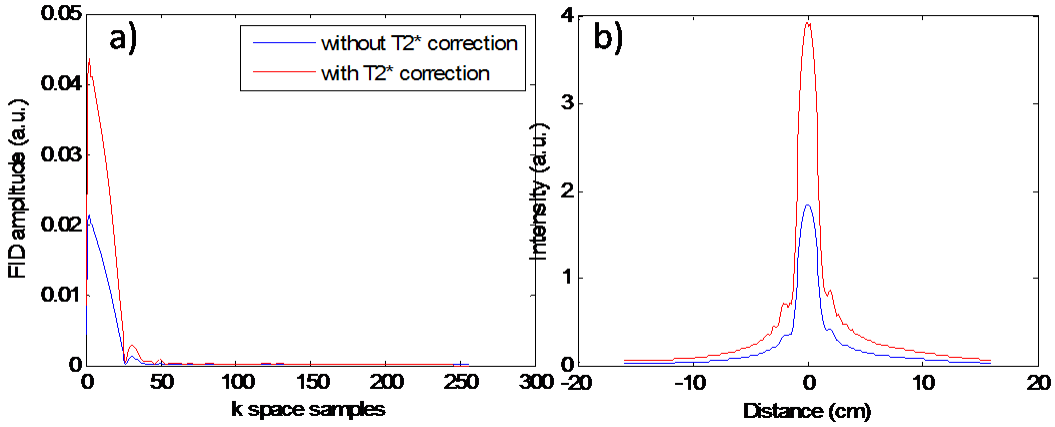

Figure 3.7: Demonstration of the T2* correction effects on the UTE signal of a rubber sample: FID (a) and projection (b) enhancement using T2* correction as defined in Chapter 2.

3.3 Application to CEA

B1 map for 20V reference input is shown in Figure 3.10. Using the average B1 value of this experiment we can estimate the achieved flip angle with linearity approximation between input transmit voltage and the B1 value. For a rectangular RF with 1V amplitude and 8ms duration, the resulting flip angle is estimated as 6^o. Note that the B1 map is generated for only the transmit channel with the higher input voltage i.e. Tx coil-1. Therefore, we must expect the magnetization to be deviated from its intended orientation depending on the RF transmitted from the second transmit channel with a lower input voltage. However, the amount of this deviation must be smaller than 10% since there is a 20dB difference between the input voltages of the transmit channels. Concurrent MRI signal is obtained by using a transmit array system to achieve the decoupling task. In the first experiments transmit coils are driven by on resonant RF waveform with rectangular envelope and 0.8mW RF input power is transmitted. In Figure 3.11, the raw data is acquired with all the gradients are turned off, meaning that signal is acquired from the whole sample. Turning on the slice selection gradient in the data acquisition chain, the MRI signal decreases in magnitude as shown in Figure 3.12. These results showing that we are able to detect MR signal during RF excitation are presented in [25,27,28]. The fluctuation voltage level observed at

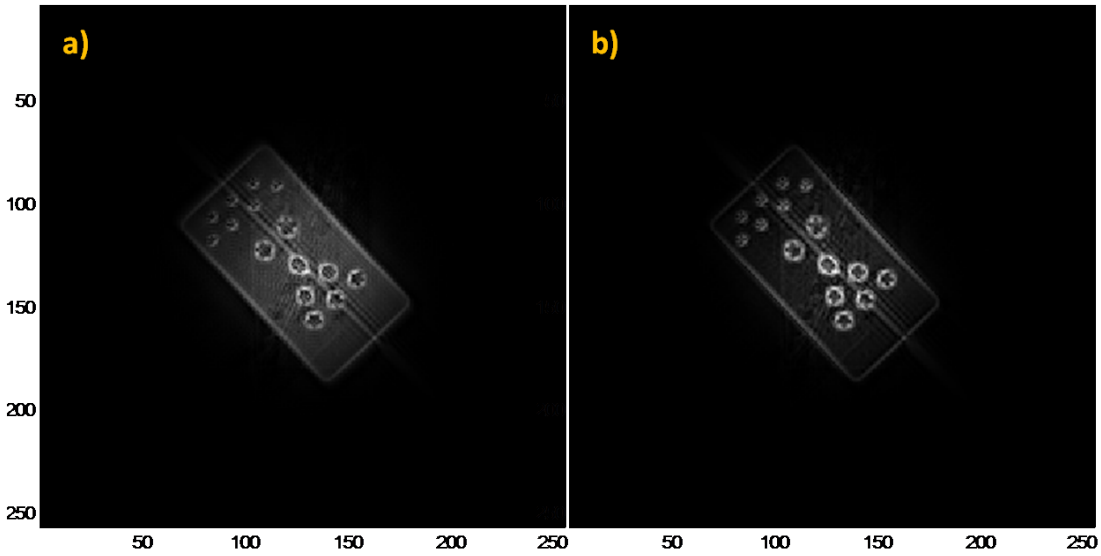

Figure 3.8: UTE image of a rubber sample for 768 projections, 240V peak RF input voltage and acquisition delay of 20μs without (a) and with T2* correction (b).

the receive coil is reduced to 30μV with the aid of geometrical decoupling. Delay of 10μs is observed between RF generator units which results in degradation of decoupling at the beginning and at the end of the RF envelope. Therefore, data acquisition is started 100μs after the RF is turned on. B1 value is estimated as 0.2μT using Bloch-Siegert shift method assuming B1 is proportional to the input RF peak to peak voltage level.

In order to increase the signal level we have inserted a 100mW LNA of 20dB gain and 2dB noise figure after the modulator output of one of the transmit channels. Figure 3.13 corresponds to the raw data for the case that small circular loop is loaded with tap water and CEA experiment is conducted for ±500Hz sweep over 40ms. We observe that when the RF passes through spins are excited and they lock into the B1 field and precess around the effective B1 as in an adiabatic slow passage experiment . For visualization of the deconvolution process Figure 3.14 shows the acquired raw data processed through leakage subtraction, a smoothing filter, and deconvolution. Deconvolution results in the FID signal in rotating frame which can be transformed either into a projection if any gradients exist during excitation or frequency spectrum containing chemical shift resonance and scalar coupling information. Figure 3.15 shows the spectrum for ethyl alcohol

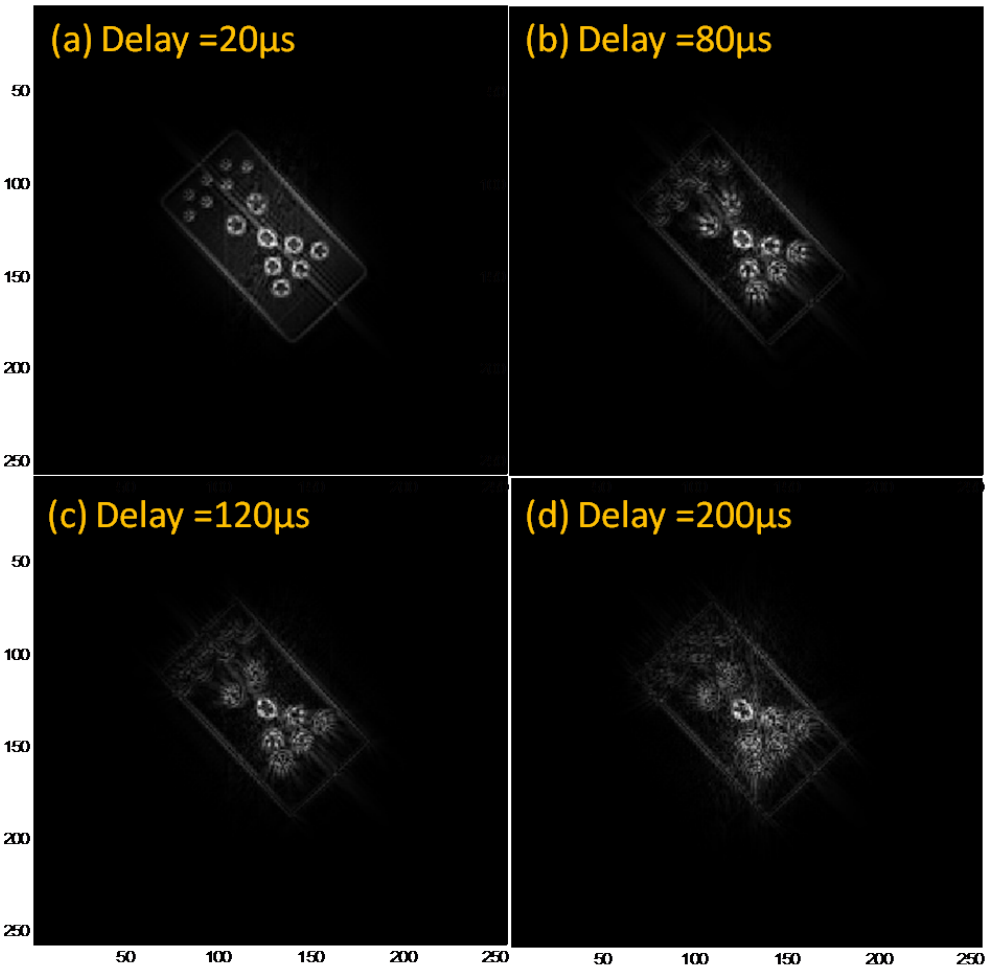

Figure 3.9: UTE image for 768 projections, 240V peak RF input voltage and acquisition delay of 20μs (a), 80μs (b), 120μs (c) and 200μs (d) .

and water solution produced for -1kHz sweep over 40ms. The acquired raw signal is difficult to interpret, yet applying deconvolution and low pass filters we could observe the chemical shift spectrum of separated hydrogen components of ethanol. This spectoscopy result is first presented in [26, 29]. 2D images for CEA sequence are shown in Figure 3.16. K space trajectories and the gridding algorithm is the same as the UTE image shown in Figure 3.6. We can observe the epoxy plate on which the Rx coil is built. Different from UTE image, here the center of k-space is not missed since the spins are not dephasing during RF excitation. Therefore, we observe a smoother image and the holes are distinctive, but the edges are lost.It should be noted that no filters or any other linear

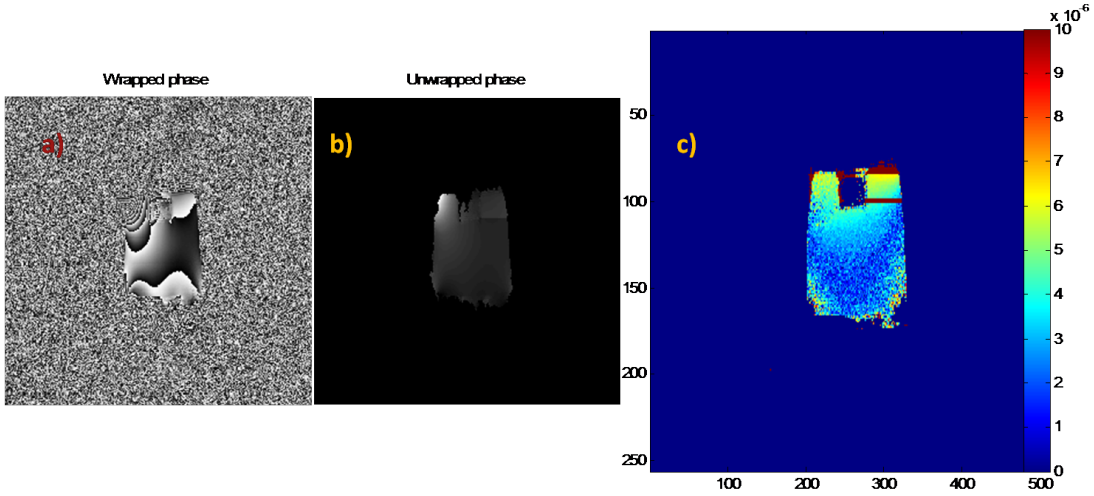

Figure 3.10: B1 map generated with Bloch-Siegert shift method for $20V_{peak}$ Fermi RF pulse with 4kHz off resonance. Decoupling setup is used with a rubber inside the glass of tap water phantom. Average B1 value is calculated as 4μT. Phase image out of the Gradient Echo based Bloch-Siegert shift sequence (a), phase image after unwrapping process (b), and calculated $|B1|$ map with masking applied (c).

operations applied to the raw data in post processing except the RF leakage subtraction and deconvolution operation. First imaging experiments are presented in [26, 29]. Increasing the input RF peak voltage to 1V, number of k space lines to 768, and the bandwidth of the chirp signal to 8kHz over 8ms for CEA experiment we observe in Figure 3.17 that the signal level increases, yet there are artifacts in the image. Another improvement is the use of Kesier-Bessel interpolation and sampling density correction for gridding operation. Use of glass coil setup helps remove undesired background signals. T2* correction as defined in UTE section was applied over the CEA signal projections as well. One of the most critical artifact source for CEA is the system stability based variations. For the B1 leakage signal that we use in the leakage subtraction we assume that the leakage is the same all over the experiment which takes 10×768 projection acquisitions. However, it is also observed during the system response estimation experiments, B1 leakage can change from measurement to measurement as shown in Figure 3.18. Therefore we have to expect some artifacts, especially low frequency artifacts due to missing leakage background signals. One way to prevent such a problem is to improve system stability. Another and more robust strategy would be to monitor

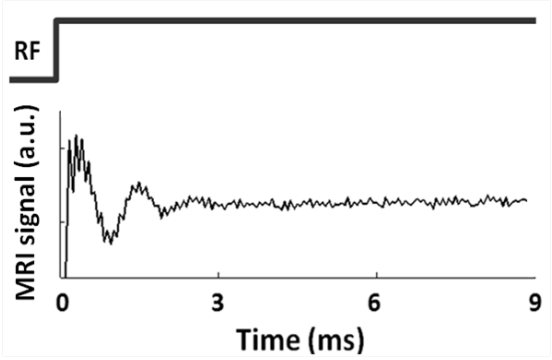

Figure 3.11: Concurrent MR signal acquired using 3T transmit array system with TR=1000 ms, Resolution =512, Acquisition BW: 50Hz/Px. This data is unprocessed raw data including B1 induced voltage signal remaining after decoupling. If leakage is higher the oscillations due to magnetization induced signal would be invisible. Since there is no gradient applied, the signal is accumulated all over the sample volume.

the RF waveform real time thorughout the experiment and use the monitored RF signal in all of the calculations that use B1 field. There is much to do for signal processing part, yet the purpose of this study is to demonstrate the feasibility of MRI with CEA and UTE techniques with the method of decoupling we have developed.

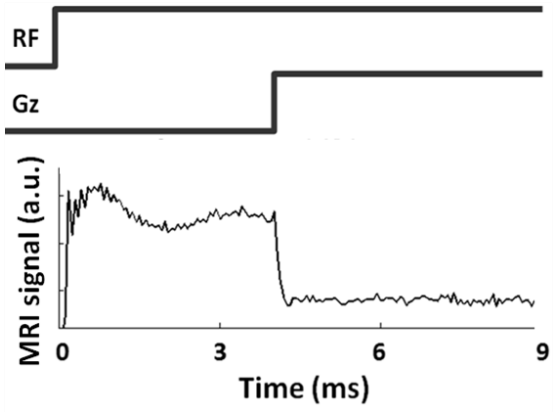

Figure 3.12: Concurrent MR signal acquired with 20mT/m slice selection gradient turned on at t=4ms. Turn on of gradient causes the signal level to drop immediately. The space encoded information can be extracted with weaker gradients and higher B1 applied. In this experiment, the input RF power was 0.8mW

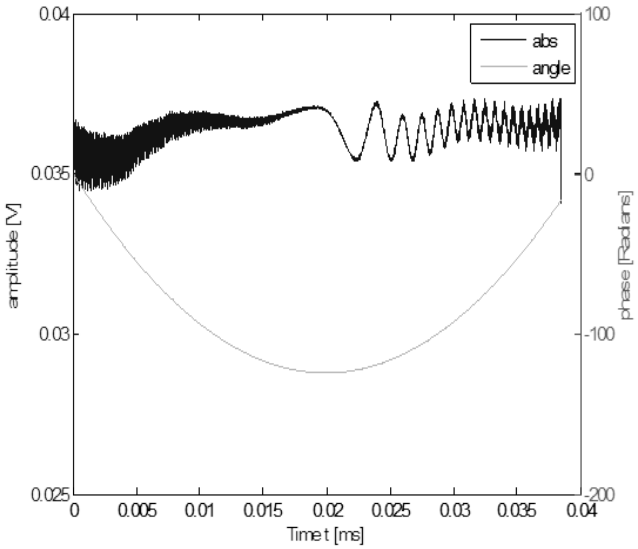

Figure 3.13: Raw data out of a CEA experiment for chirp B1 excitation of ±500Hz over 40ms observed in water phantom.

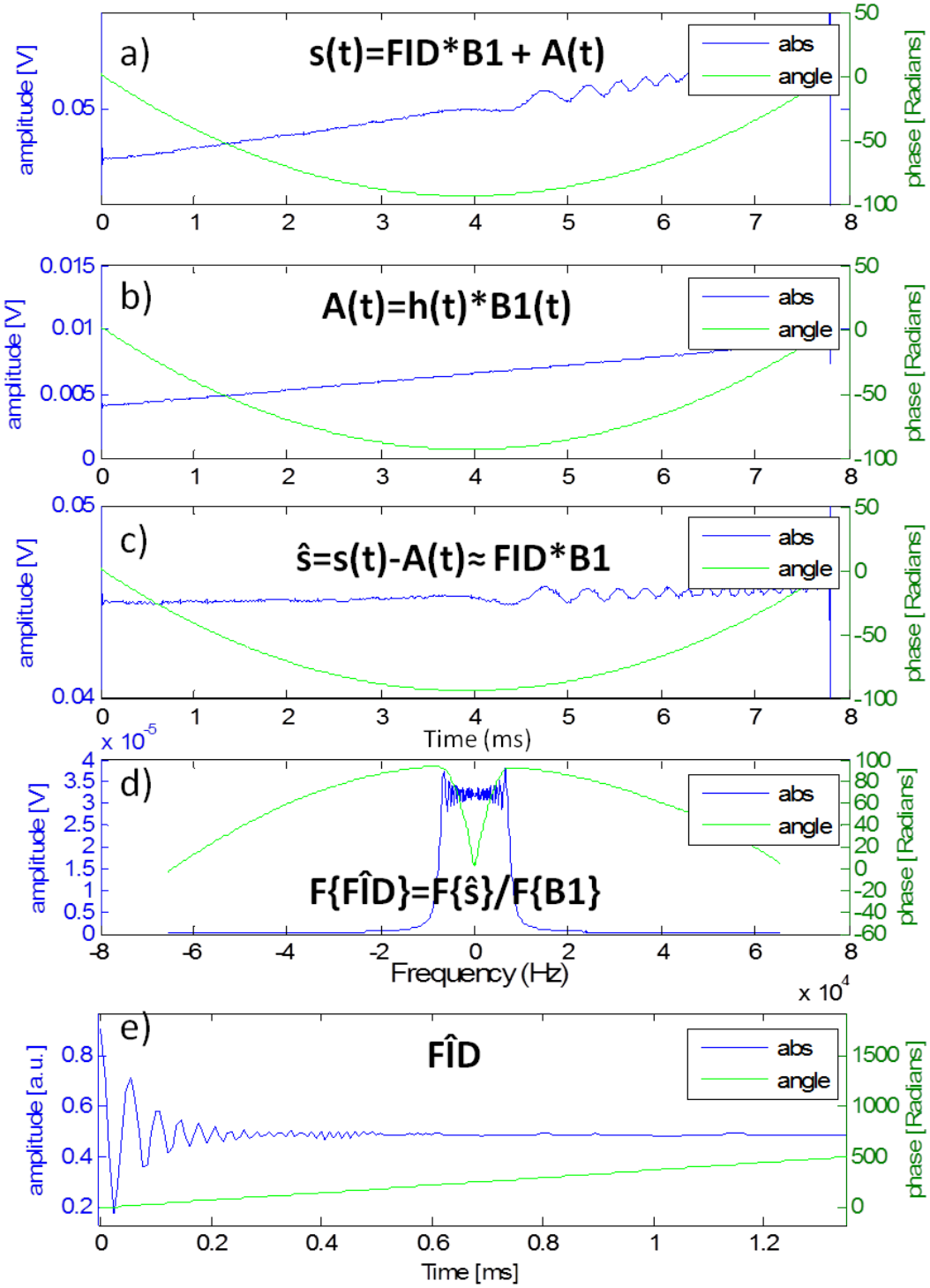

Figure 3.14: Acquired raw data from a water sample (a). Input B1 waveform as a chirp function (b). Acquired signal after the leakage subtraction (c). Fourier transform of the estimated FID signal after deconvolution (d) and single-sided FID signal which is an approximation of the actual FID (e).

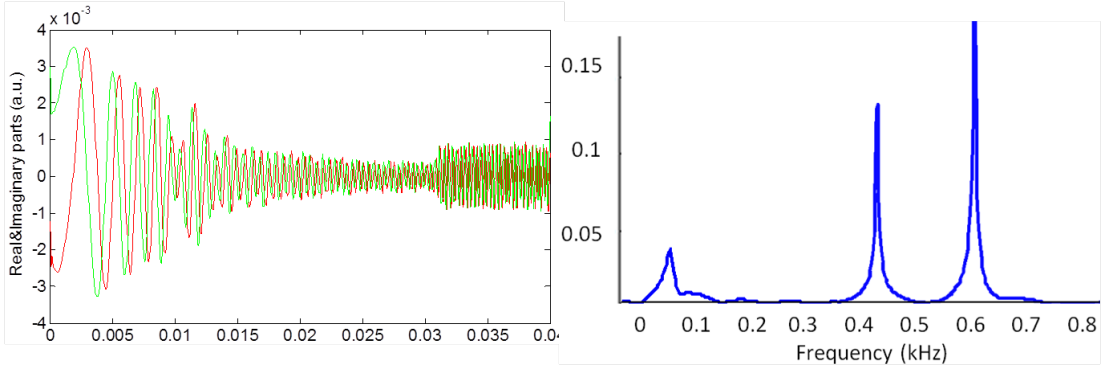

Figure 3.15: Raw data acquired from ethanol sample (a). Chemical shift spectrum obtained after deconvolution (b).

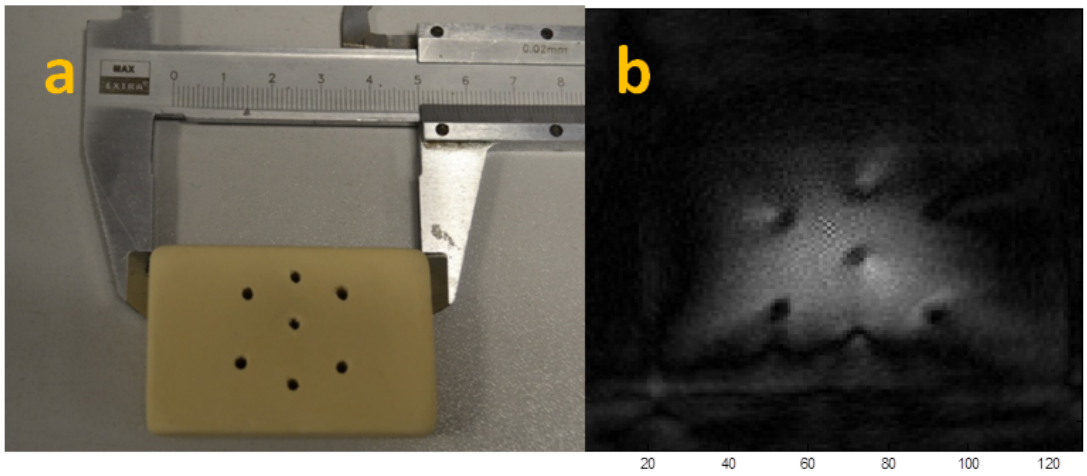

Figure 3.16: Rubber phantom of T2 of 500μs with holes (a). CEA image (b).

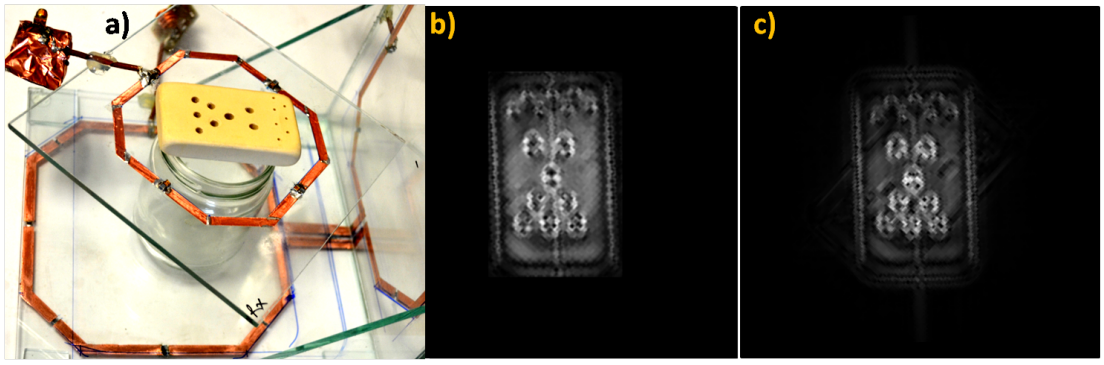

Figure 3.17: Rubber phantom of T2 of 500μs with holes (a). CEA image with improved imaging parameters and gridding with Keiser-Bessel interpolation (b), and T2* correction applied (c).

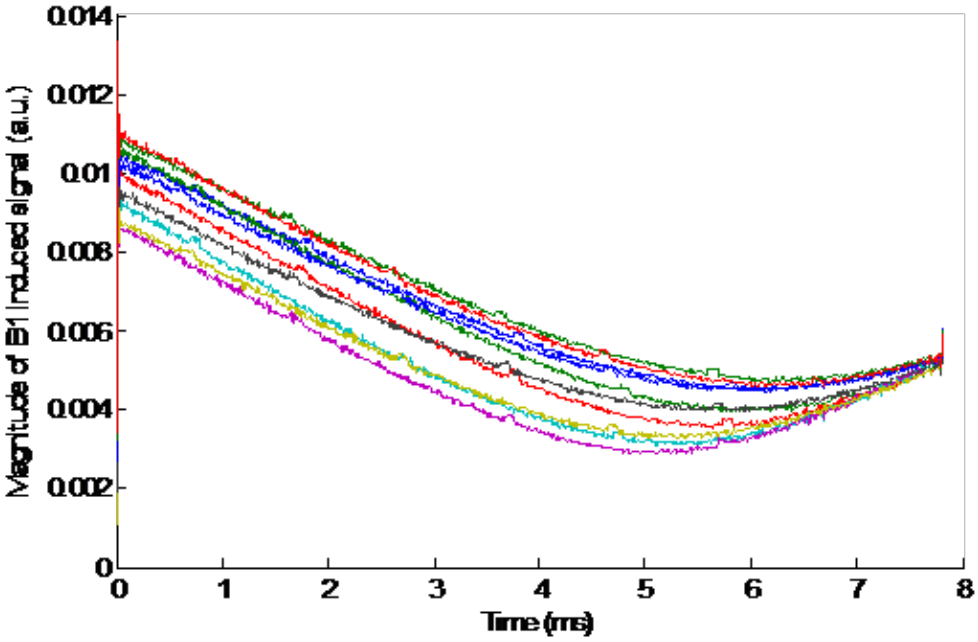

Figure 3.18: B1 induced leakage signal variation over subsequent measurements after decoupling is preceeded. The measurements are taken subsequently with 1min intervals while keeping everything unchanged.

Chapter 4

Discussions

Decoupling performance depends strictly on the sensitiveness of the rotation setup and the degree of precision of the RF generator phase adjustment unit. Transmit noise has become a significant factor in our system. In the experiments we excluded RF power amplifiers from the setup because the amplifiers add noise during transmission. Our aim is to implement spectroscopy and imaging of samples with ultra-short T2* using CEA without being limited to gapped pulse sequences or frequency sweep approaches. Using the method presented in this study both RF excitation and signal acquisition can be set on resonant. This method provides wide range flexibility for the applied RF field. As long as multiple transmit elements with controllable phase and amplitude are used, magnetic field decoupling can be achieved. Dynamic range requirement is also lower compared to other isolation methods.

Use of more than two transmit coils would help further reduction of remaining B1 induced voltage after multiport decoupling. However, coupling between transmit coils should also be considered carefully before such an advancement. Decoupling with two transmit coils is proceeded with experimental methods. However, some preliminary studies using numerical simulations or approximate analytical solutions that would help us to understand decoupling problem including more than two transmit coil elements.

The methods for isolation between the MR signal and the B1 induced voltage

signal suffer from being too much motion sensitive, in general. Object motion during acquisition does not only cause motion artifacts but also the decoupling performance changes due to the changes in coil impedance. Therefore, the object motion should be minimized in CEA applications. Object motion can be observed as changes in coil impedances. Variation of coil impedances results in variations of B1 induced voltage between subsequent acquisitions. Therefore, real-time recording of excitation RF field is necessary for an automatic reconstruction process suitable to pre-clinical and clinical applications.

The current system is to be optimized and modified to make its use convenient in research and for clinical purposes. For in vitro measurements and spectroscopy studies, a motor controlled rotation mechanism receiving a feedback about the magnetic fields can be used. However, for clinical use and in vivo measurements, it is not feasible to rotate patients and therefore the system design must be modified appropriately. For that purpose, transmit coils can be rotated around the patient. More feasible transmit coil design would be using a transmit array of N channels where N small coils are driven by embedded RF generator units which can be FPGA controlled. Geometrical decoupling could be achieved by selection of appropriate coil sets and multiport decoupling can easily be achieved using the remaining elements of the transmit coil array. This design has advantages over others for not having a moving part inside the scanner. Besides, small transmit coils upgrades linearity of the transmit field and the multiport decoupling increases the amount of decoupling compared to decoupling with two transmitting coils.

The effect of transmit coil with weaker B1 field on the MRI signal can be observed as a residual in the magnitude of the magnetization. We did not include this effect in our analysis assuming that it is a minor effect. However, the effect of multiple coil transmission on the magnetization vector must be analyzed in detail for a more rigorous treatment of the acquired signal.

Gradients forming the radial k-space trajectory can be designed such that instead of switching gradients on and off to acquire projections along different radial directions, by changing gradient levels only, the same projections could be acquired. If the gradient level is changed immediately after one projection is acquired and kept on for a certain time interval until the next acquisition starts, spins that

are excited will be spoiled and the effect of the previous excitation will not last during the next excitation. This continuous gradient approach can be applied to 2D and 3D imaging with k space trajectories that do not necessitate switching the gradients on and off. Such a gradient design would eliminate the acoustic noise in MRI scans significantly.

Other than thermal noise, there may be some other interference causing distortions in the transmitted RF signal that we are not able to point out explicitely. Some of the distortion sources might be voltage fluctuations, modulator based frequency shifts, phase noises based on oscillator infidelities, and cable interferences. Such distortions and noise are hard to deal with when they are emitted from independent sources. Different RF sources have different noise characteristics implying that although we reduce the induced voltage through decoupling, we may not be able to reduce the noise, but increase the noise. As a result, the system introduced in this work is hard to implement using standard MRI systems and needs particular design considerations addressing all these challenges. Use of a single RF generator unit with a power splitter is a useful approach that cancels RF generator unit based abnormalities. For example, field of two transmit coils fed up by one RF generator unit with a power splitter will cancel the abnormalities as well as magnetic fields coupled in the receiver coil because identical abnormalities are delivered to both coils. Such a system would allow to work with higher RF input powers with our system being more tolerated to the noise introduced by the transmit sources.

We have demonstrated the UTE and CEA sequences using a transmit array system and the decoupling over 70dB is achieved which eliminates the need for a detuning diode in the receive coil. Subtraction of MRI signal and B1 induced voltage is still required for image reconstruction of CEA. Advantages of CEA sequence are that it has much lower peak power and true zero echo time. Use of very low RF input powers could also be significant for some applications. The isolation method presented in this work is a potential solution to receiver dynamic range problems in implementation of CEA. Further isolation between MR signal and RF is achieved compared to other methods.

Improving the decoupling, signal level in CEA experiments will be increased significantly. The system introduced in this work stands for a promising system

for implementation of NMR applications such UTE, CWNMR; and a powerful alternative for recently proposed CEA methods such as sideband excitation and continuous SWIFT.

Time interleaved approach in MRI results in limitations in echo time due to gradient and RF coil switching times, coil ring down times and acquisition bandwidth. The idea of concurrent excitation and acquisition overcomes these problems due to its intrinsic property of zero echo time. CEA using magnetic field decoupling with transmit array enables the detection of on resonant MRI signal during on resonant excitation. Therefore, there will be no need for RF coils to be turned off but the receiver unit can acquire signal at any time point and acquisition bandwidth is not limited. In addition, CEA provides us with the knowledge of spin properties during excitation. Since excitation lasts much shorter than the relaxation, imaging using spin parameters identifying excitation characteristics will take shorter in time.

Chapter 5

Conclusions

In this study, a new method for decoupling of coils is introduced and the use of this method in concurrent radio frequency (RF) excitation and MRI signal reception is demonstrated. This study shows that RF signal coupled in the receive coils can be reduced by more than 70dB using a transmit array system of two transmit elements. MR signal can be detected directly independent from the shape of RF. Subtraction of MRI signal and the B1 induced voltage is still required for image reconstruction. Preliminary results indicate that this isolation method is potentially useful in MRI and spectroscopy applications requiring concurrent excitation and acquisition (CEA) and/or zero echo time as well as it can be used as an additional decoupling procedure to the existing decoupling methods. The isolation method presented in this work is a potential solution to the receiver dynamic range problems in implementation of CEA. Further reduction of on resonant B1 induced voltage is achieved compared to that is achieved using other methods. It is also demonstrated that the acquisition delay in ultra short echo time (UTE) techniques can be reduced using this method of decoupling.

Significance of CEA reveals itself in the limits where UTE methods are insufficient such as solids and tightly bounded water in bones. Currently, MRI field is seeking for the best short T2* imaging method. There are many short T2* imaging methods suggested such as UTE [5], ZTE [15], SWIFT [12], WASPI [42], SPI [43] and so on. CEA is supposed to be an alternative to these despite its challenges

in implementation some which are stated in this thesis and few are resolved. The decoupling method we have developed is not restricted to use in CEA or the potential use in UTE. It presents a novel approach to get benefit from transmit array opportunity in MRI where we have transmit set of coils, decoupling set of coils and receive coils. This method can find other applications where B1 induced currents are needed to be decreased without changing the sensitivity of the transmit field.

Bibliography

[1] P. Gatehouse and G. Bydder, "Magnetic resonance imaging of short T_2 components in tissue," *Clinical radiology*, vol. 58, no. 1, pp. 1–19, 2003.

[2] M. A. Schmidt, G.-Z. Yang, P. D. Gatehouse, and D. N. Firmin, "FID-based lung mri at 0.5 T: Theoretical considerations and practical implications," *Magnetic resonance in medicine*, vol. 39, no. 4, pp. 666–672, 1998.

[3] D. J. Tyler, M. D. Robson, R. M. Henkelman, I. R. Young, and G. M. Bydder, "Magnetic resonance imaging with ultrashort TE (UTE) pulse sequences: technical considerations," *Journal of Magnetic Resonance Imaging*, vol. 25, no. 2, pp. 279–289, 2007.

[4] D. Lurie, S. McCallum, J. Hutchison, and M. Alecci, "Continuous-wave NMR imaging of solids.," *MAGMA*, vol. 4, no. 1, pp. 77–81, 1996.

[5] M. D. Robson, P. D. Gatehouse, M. Bydder, and G. M. Bydder, "Magnetic resonance: an introduction to ultrashort TE (UTE) imaging," *Journal of computer assisted tomography*, vol. 27, no. 6, p. 825, 2003.

[6] P. C. Lauterbur *et al.*, "Image formation by induced local interactions: examples employing nuclear magnetic resonance," *Nature*, vol. 242, no. 5394, pp. 190–191, 1973.

[7] R. R. Ernst, G. Bodenhausen, A. Wokaun, *et al.*, *Principles of nuclear magnetic resonance in one and two dimensions*, vol. 14. Clarendon Press Oxford, 1987.

[8] R. K. Gupta, J. A. Ferretti, and E. D. Becker, "Rapid scan Fourier transform NMR spectroscopy," *Journal of Magnetic Resonance (1969)*, vol. 13, no. 3, pp. 275–290, 1974.

[9] D. E. Demco and B. Blümich, "Solid-state NMR imaging methods. Part 1: Strong field gradients," *Concepts in Magnetic Resonance*, vol. 12, no. 4, pp. 188–206, 2000.

[10] I. J. Lowe, "Free Induction Decays of Rotating Solids," *Physical Review Letters*, vol. 2, pp. 285–287, Apr. 1959.

[11] D. Cory, J. De Boer, and W. Veeman, "Magic-angle spinning proton NMR imaging of polybutadiene/polystyrene blends," *Macromolecules*, vol. 22, no. 4, pp. 1618–1621, 1989.

[12] D. Idiyatullin, C. Corum, J.-Y. Park, and M. Garwood, "Fast and quiet MRI using a swept radiofrequency," *Journal of Magnetic Resonance*, vol. 181, no. 2, pp. 342–349, 2006.

[13] J. Du, "Imaging bone water compartments," in *International Society of Magnetic Resonance in Medicine 21.*

[14] J. Rahmer, P. Bornert, J. Groen, and C. Bos, "Three-dimensional radial ultrashort echo time imaging with T_2 adapted sampling," *Magnetic resonance in medicine*, vol. 55, no. 5, pp. 1075–1082, 2006.

[15] M. Weiger, K. P. Pruessmann, and F. Hennel, "MRI with zero echo time: hard versus sweep pulse excitation," *Magnetic Resonance in Medicine*, vol. 66, no. 2, pp. 379–389, 2011.

[16] C. Corum, A. Babcock, D. Idiyatullin, A. L. Snyder, D. Hutter, L. Everson, M. Nelson, and M. Garwood, "The utility of sweep imaging with fourier transform (SWIFT) in breast cancer," in *Proceedings International Society of Magnetic Resonance in Medicine 20.*

[17] R. Chamberlain, S. Moeller, C. Corum, D. Idiyatullin, and M. Garwood, "Quiet T_1 and T_2-weighted brain imaging using SWIFT," in *Proceedings International Society of Magnetic Resonance in Medicine 19.*

[18] S. Mangia, R. Chamberlain, F. Martino, S. Moeller, C. Corum, T. Kim, C. Kalavagunta, S. Michaelli, M. Garwood, S. Kim, and K. Ugurbil, "Functional MRI with SWIFT," in *Proceedings International Society of Magnetic Resonance in Medicine 20*.

[19] L. Lehto, A. Sierra, C. Corum, D. Idiyatullin, A. Pitkanen, M. Garwood, and O. Grohn, "SWIFT imaging of myelin loss in traumatic brain injury in rats," in *Proceedings International Society of Magnetic Resonance in Medicine 20*.

[20] L. Lehto, C. Corum, D. Idiyatullin, P. A, M. Garwood, O. Grohn, and A. Sierra, "Iron imaging using SWIFT in a rat model of traumatic brain injury," in *Proceedings International Society of Magnetic Resonance in Medicine 20*.

[21] R. Chamberlain, M. Etheridge, D. Idiyatullin, C. Corum, C. Bischof, and M. Garwood, "Measuring T_1 in the presence of very high iron concentrations with SWIFT," in *Proceedings International Society of Magnetic Resonance in Medicine 20*.

[22] D. Idiyatullin, S. Suddarth, C. Corum, G. Adriany, and M. Garwood, "Continuous SWIFT," in *Proceedings International Society of Magnetic Resonance in Medicine 19*.

[23] O. Brunner, B. E. Dietrich, M. Pavan, and K. Pruessmann, "MRI with sideband excitation: Application to continuous SWIFT," in *Proceedings International Society of Magnetic Resonance in Medicine 20*.

[24] D. Idiyatullin, S. Suddarth, C. Corum, G. Adriany, and M. Garwood, "Continuous SWIFT," *Journal of Magnetic Resonance*, 2012.

[25] A. C. Ozen, N. K. Ertan, and E. Atalar, "Detection of MR signal during RF excitation using a transmit array system," in *Proceedings International Society of Magnetic Resonance in Medicine 20*.

[26] A. C. Ozen and E. Atalar, "Decoupling of transmit and receive coils using a transmit array system: Application to UTE and CEA," in *Proceedings International Society of Magnetic Resonance in Medicine 21*.

[27] A. C. Ozen and E. Atalar, "Verici dizisi kullanılarak manyetik rezonans sinyalinin RF uyarımı sırasında saptanması," in *Türk Manyetik Rezonans Derneği Yıllık Toplantısı 17*.

[28] A. C. Ozen and E. Atalar, "Magnetic resonance imaging and spectroscopy with concurrent excitation and acquisition using a transmit array system," in *International Summer School on Biomedical Imaging 6*.

[29] A. C. Ozen and E. Atalar, "Implementation of MRI and NMR spectroscopy with concurrent excitation and acquisition using a transmit array system," in *Proceedings Experimental Nuclear Magnetic Resonance Conference 54*.

[30] R. Ludwig, *RF Circuit Design: Theory & Applications, 2/e*. Pearson Education India, 2000.

[31] J. I. Jackson, C. H. Meyer, D. G. Nishimura, and A. Macovski, "Selection of a convolution function for Fourier inversion using gridding," *Medical Imaging, IEEE Transactions on*, vol. 10, no. 3, pp. 473–478, 1991.

[32] S. Ljunggren, "A simple graphical representation of Fourier-based imaging methods," *Journal of Magnetic Resonance (1969)*, vol. 54, no. 2, pp. 338 – 343, 1983.

[33] J. D. Roberts, "The Bloch equations. How to have fun calculating what happens in NMR experiments with a personal computer," *Concepts in Magnetic Resonance*, vol. 3, no. 1, pp. 27–45, 1991.

[34] J. Pauly, D. Nishimura, and A. Macovski, "A k-space analysis of small-tip-angle excitation," *Journal of Magnetic Resonance (1969)*, vol. 81, no. 1, pp. 43–56, 1989.

[35] J. Dadok and R. F. Sprecher, "Correlation NNW spectroscopy," *Journal of Magnetic Resonance (1969)*, vol. 13, no. 2, pp. 243–248, 1974.

[36] R. A. De Graaf, *In vivo NMR spectroscopy: principles and techniques*. Wiley-Interscience, 2008.

[37] A. J. Fagan, G. R. Davies, J. Hutchison, F. P. Glasser, and D. J. Lurie, "Development of a 3-D, multi-nuclear continuous wave NMR imaging system," *Journal of Magnetic Resonance*, vol. 176, no. 2, pp. 140–150, 2005.

[38] A. Tannus and M. Garwood, "Adiabatic pulses," *NMR in Biomedicine*, vol. 10, no. 8, pp. 423–434, 1997.

[39] L. I. Sacolick, F. Wiesinger, I. Hancu, and M. W. Vogel, "B1 mapping by Bloch Siegert shift," *Magnetic Resonance in Medicine*, vol. 63, no. 5, pp. 1315–1322, 2010.

[40] A. E. Turk, Y. Z. Ider, A. S. Ergun, and E. Atalar, "Fourier domain approximation for Bloch Siegert shift," in *Proceedings International Society of Magnetic Resonance in Medicine 21*.

[41] A. E. Turk, Y. Z. Ider, and E. Atalar, "Analysis of B1 mapping by Bloch Siegert shift," in *Proceedings International Society of Magnetic Resonance in Medicine 20*.

[42] Y. Wu, J. L. Ackerman, D. A. Chesler, L. Graham, Y. Wang, and M. J. Glimcher, "Density of organic matrix of native mineralized bone measured by water-and fat-suppressed proton projection MRI," *Magnetic resonance in medicine*, vol. 50, no. 1, pp. 59–68, 2003.

[43] S. Beyea, B. Balcom, T. Bremner, P. Prado, A. Cross, R. Armstrong, and P. Grattan-Bellew, "The influence of shrinkage-cracking on the drying behaviour of white portland cement using single-point imaging (SPI)," *Solid state nuclear magnetic resonance*, vol. 13, no. 1, pp. 93–100, 1998.

[44] Y. Eryaman, "Design and implementation of internal MRI coils using ultimate intrinsic SNR," Master's thesis, Bilkent University.

[45] B. Akin, Y. Eryaman, and E. Atalar, "A method for phantom conductivity and permittivity measurements," in *Proceedings European Society of Magnetic Resonance in Medicine and Biology 26*.

[46] A. C. Ozen, B. Akin, and E. Atalar, "Fantomların dielektrik özelliklerinin belirlenmesi için pratik bir ölçüm tekniği ve bağlantı düzeneği," in *Türk Manyetik Rezonans Derneği Yıllık Toplantısı 16.*

[47] V. Acikel, O. Ulutan, A. C. Ozen, B. Akin, Y. Eryaman, and E. Atalar, "A novel MRI based electrical properties measurement technique," in *International Society of Magnetic Resonance in Medicine 21.*

[48] V. Acikel and E. Atalar, "Modeling of radio-frequency induced currents on lead wires during MR imaging using a modified transmission line method," *Medical Physics*, vol. 38, no. 12, p. 6623, 2011.

[49] C. Gabriel, S. Gabriel, and E. Corthout, "The dielectric properties of biological tissues: 1. literature survey," *Physics in medicine and biology*, vol. 41, no. 11, p. 2231, 1996.

[50] M. A. Stuchly and S. S. Stuchly, "Coaxial line reflection methods for measuring dielectric properties of biological substances at radio and microwave frequencies-a review," *Instrumentation and Measurement, IEEE Transactions on*, vol. 29, no. 3, pp. 176–183, 1980.

[51] T. W. Athey, M. A. Stuchly, and S. S. Stuchly, "Measurement of radio frequency permittivity of biological tissues with an open-ended coaxial line: Part 1," *Microwave Theory and Techniques, IEEE Transactions on*, vol. 30, no. 1, pp. 82–86, 1982.

[52] M. D. Janezic and J. A. Jargon, "Complex permittivity determination from propagation constant measurements," *Microwave and Guided Wave Letters, IEEE*, vol. 9, no. 2, pp. 76–78, 1999.

[53] G. Giovannetti, F. Frijia, L. Menichetti, V. Hartwig, V. Viti, and L. Landini, "An efficient method for electrical conductivity measurement in the RF range," *Concepts in Magnetic Resonance Part B: Magnetic Resonance Engineering*, vol. 37B, no. 3, pp. 160–166, 2010.

[54] D. M. Pozar, *Microwave engineering.* John Wiley Sons, 2009.

Appendix A

Measurement of Dielectric Properties

In this section, dielectric measurement device we built and the measurement method we developed for accurate measurement of dielectric properties of liquid and gel materials within radio frequency range up to 500MHz will be described along with some sample measurement results. This project is started by the efforts of my former colligues in UMRAM and partly presented in master's thesis work of Yiğitcan Eryaman [44], an abstract submitted to ESMRMB annual meeting by Burak Akın [45], an abstract submmitted to TMRD annual meeting [46], and finally an abstract submitted to ISMRM annual meeting [47] where our work on dielectric measurement device is compared with another method developed in UMRAM by Volkan Açıkel called MOTLiM [48]. In this section I will be mostly pointing out my contributions to this research project. The theory and the measurement fixture was already developed when I started working on the project. I have contributed to develop a better model of the fixture by modeling the parts of the fixture which are not included in the previous formulation as lumped elements so that the estimations get closer to the measurements. I have also develop a software in MATLAB® based on optimization algorithms so that more precise estimations are obtained within a shorter time interval compared to the old for-loop based estimation algorithm. I have conducted many measurement

experiments and also attempted to measure dielectric properties of in vitro blood sample obtained from a lab rat.

A.1 Introduction

Measurement of permittivity and conductivity in RF range is significant for electromagnetic dosimetry studies where realistic models for in-vivo electromagnetic energy exposures are simulated and internal fields within animals are calculated. There has been a considerable research effort on accurate measurement methods of complex relative permittivity as well on formation of a reliable data base for in-vivo and in-vitro measurement results [49].

There are measurement techniques for complex permittivity calculations mostly relying on open-ended coaxial line structures. However, the approach to the problem shows diversity [50]. One of the techniques is based on capacitive modeling of the coaxial line and measures the change in the fringing field due to sample contact [51]. There are also calculations based propagation constant measurements [52]. A recently proposed method for conductivity measurement in RF range looks at the change in the impedance seen by an RF coil in loaded condition [53].

We have developed reflection coefficient based measurement technique for lossy transmission line models to determine relative permittivity and conductivity simultaneously. We constructed a coaxial line fixture that is optimized to provide maximum sensitivity to changes in permittivity and conductivity at 123MHz. Our measurement method employs a fitting and optimization process based on multiple measurements of various amount of samples put in the fixture ensuing a better accuracy compared to single measurement based methods. We describe our setup, permittivity and conductivity calculation program, and finally we present some measurement results.

A.2 Theory

The dielectric properties of materials are expressed by complex relative permittivity as in equation A.1

$$\varepsilon = \varepsilon^{'} - j\varepsilon^{''} \tag{A.1}$$

$$\varepsilon^{''} = \frac{\sigma}{\varepsilon_o \omega} \tag{A.2}$$

where ε' is the relative permittivity of the material and ε" is the out-of-phase loss factor associated with its total electrical conductivity σ with frequency dependence.

We employed lossy transmission line model with a series inductance and a resistance and a parallel capacitance and a conductance which relates the characteristic impedance of the transmission line to relative permittivity and conductivity. We think of filled and empty parts of the coaxial line as if they are separate lines connected in series as shown in Figure A.1. We can express the impedance and the reflection coefficients as in equation A.3 [54].

$$\begin{aligned} Z_2 &= \frac{Z_o}{j\tan(\beta\iota_1)} \\ Z_1 &= Z_{o2}\frac{Z_2 + Z_{o2}\tanh(\beta\iota_2)}{Z_{o2} + Z_2\tanh(\beta\iota_2)} \\ \beta &= \omega\sqrt{LC} \end{aligned} \tag{A.3}$$

where Z_o is the characteristic impedance of the empty part of the transmission line and Z_{o2} is that of the filled part of the line.

Measured reflection coefficient is shown in equation A.4 assuming that the input impedance of the network analyzer is 50 Ω.

$$\Gamma = \frac{Z_1 - 50}{Z_1 + 50} \tag{A.4}$$

A.3 Material and Methods

We constructed a coaxial line fixture and generated a realistic model of it using Advanced Design Systems® (ADS) including connection points and conductor

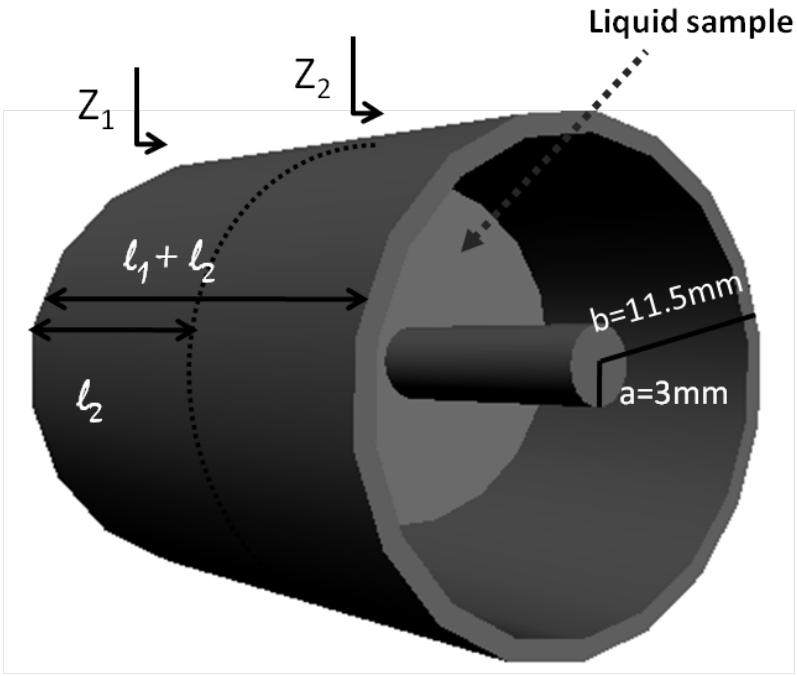

Figure A.1: Schematic of coaxial fixture. The transmission line is modeled as two series lumped element model of a coaxial line one which has a lossy medium inside while the other one is filled with air. Dimensions are given. The length vector of pouring the sample inside the fixture is calculated and entered in the optimization program as input along with the measured reflection coefficient data.

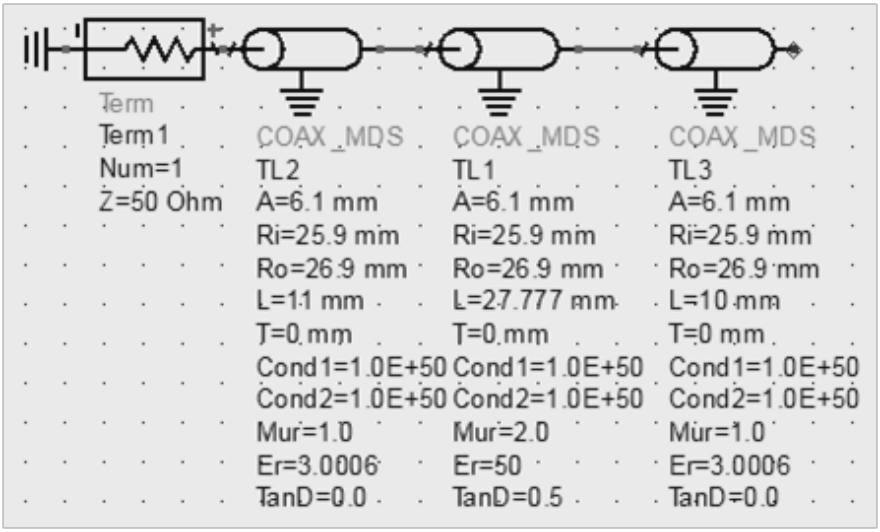

Figure A.2: Realistic model of the fixture is created using ADS®. Physical dimensions are measured with high precision micrometers. The part of the fixture that is filled with derlin is also considered in this model. Test for the optimization program written in MATLAB® is done using s-parameter simulations out of the ADS® using realistic model.

resistance as shown in Figure A.2. We have included third part into the model which accounts for 1cm length the fixture section with Delrin inside ($\varepsilon_r = 3$). Dimensions were optimized for sensitivity of the measured reflection coefficient to the changing liquid length. This model with realistic parameters is introduced to MATLAB® as a function that yields the reflection coefficient as an output given relative permittivity, conductivity and the liquid length as inputs. An additional series inductance is included in the model to account for the extension of the inner conductor reaching towards the BNC connector. Calibration of the network analyzer is a significant component for the accuracy of the measurements. Using port extension option in the network analyzer (Agilent E5061A) the impedance seen through the empty fixture is set to the same value as the realistic model result for a better fit of the data. Liquid is filled in the fixture using a pipette by 0.5ml samples where the experimental setup is shown in Figure A.3. With each sample is filled in, measured reflection coefficient is saved for the desired frequency range and then this data is read by a MATLAB® routine. Using the optimization tool inherent in MATLAB®, measured reflection coefficients are fit to appropriate relative permittivity and conductivity values that minimizes the

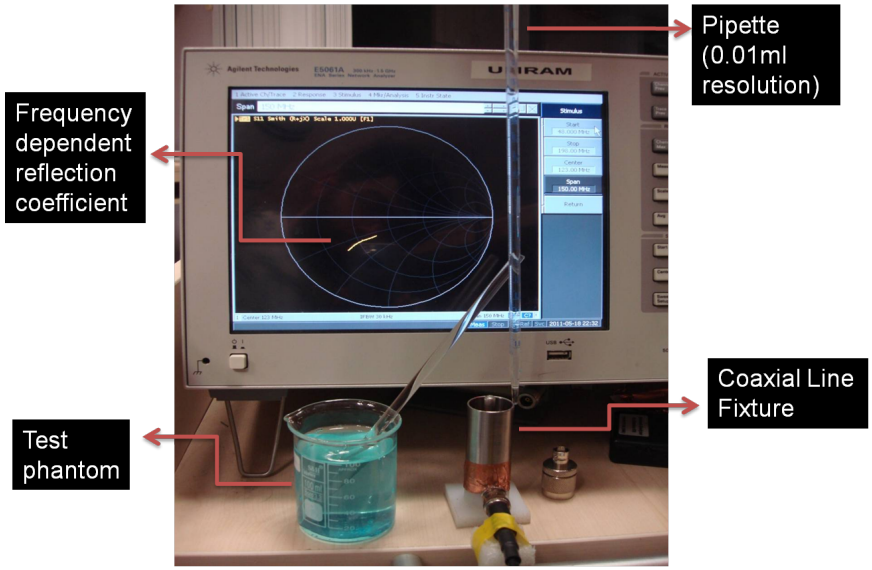

Figure A.3: Picture of experimental setup. The collection of data is done as follows. First the network analyzer is calibrated properly in a desired frequency range taking the impedance of the empty fixture into account. Test phantom is prepared and samples are gathered using a pipette and poured into the fixture in desired amount. At each step the reflection coefficients are recorded. In recent measurements an automatic pipette is used which is found to be very convenient and time efficient.

Frequency (MHz)	Solute (per lt water)	Relative permittivity	Conductivity (S/m)
123.5	1 gr NaCl	61.9	0.145
123.5	1 gr NaCl + 1 gr $CuSO_4$	62.7	0.193
123.5	2 gr NaCl	66.8	0.346
64	1 gr NaCl	75.9	0.198
64	1 gr NaCl + 1 gr $CuSO_4$	74.0	0.249
64	2 gr NaCl	71.0	0.378

Figure A.4: Results for dielectric measurements of some ionic solutions.

difference between the experimental and theoretical reflection coefficient values at the desired frequency.

A.4 Results

Water solutions of different concentrations of NaCl and CuSO4 are measured for their dielectric properties at two different frequencies: 123.5MHz and 64MHz corresponding to Larmour frequencies at 3T and 1.5T static magnetic field, respectively. The results are shown in Figure A.4. In-vitro rat blood sample measurements are also done. At 123.5MHz ε_r=46.2 and σ=1.05S/m; at 64MHz ε_r=67.5 and σ=0.955S/m.

Frequency dependence of the conductivity can be observed in Figure A.5 for different concentrations of NaCl-water solutions and in Figure A.6 for varying concentrations of CuSO4-water solutions. Subsequent measurement of the same samples produced less than 0.3"%" error in ε_r and σ values.

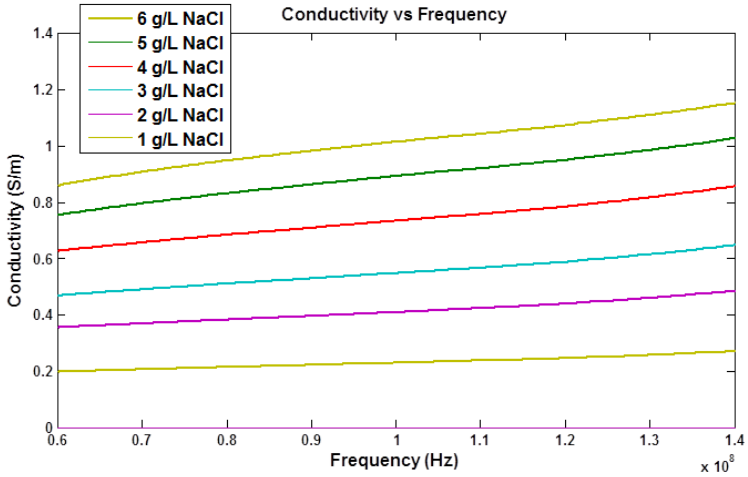

Figure A.5: Frequency versus conductivity is plotted using real measurements for 6 different concentrations of NaCl and water solutions. Data is acquired between 60MHz and 140MHz. The bottom line shows conductivity of pure water. Conductivity and permittivity for a wide range of frequencies can be measured at one experiment. This is a very important facility since there will be no need for interpolation of the data due to lack of data at needed frequencies. Interpolation can result in computation errors because the assumption linear dependence to the frequency can be problematic specially if the interpolation range is long.

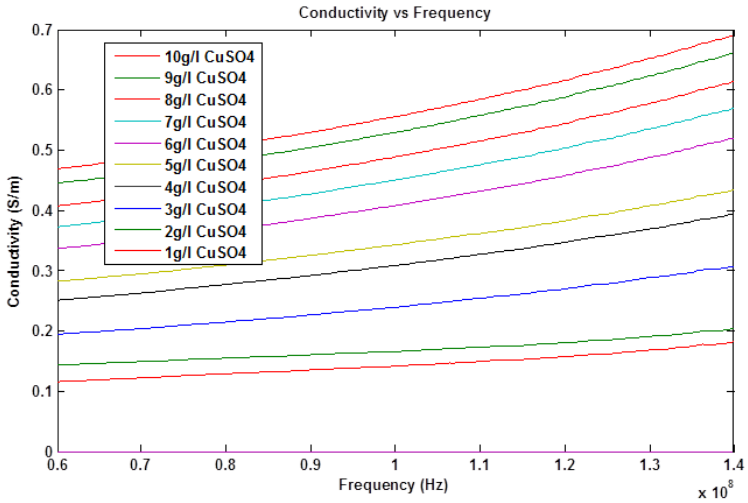

Figure A.6: Frequency vs. conductivity for CuSO4 and water solution of different concentrations. It is critical to form a data base for frequency and concentration dependent dielectric properties of materials that one can use this data base to produce a phantom of desired dielectric properties which could be used in safety experiments resulting in more reliable outputs.

A.5 Conclusions

In this study a measurement technique for determination of dielectric properties is implemented with a cheap and practical setup. We have shown that solutions of various relative permittivity and conductivity can be prepared by adjusting the type and concentrations of the solutes inside. This property can be used for preparation of MRI test phantoms that mimics dielectric properties of human tissue and organs. Accurate knowledge of dielectric properties play significant role in MRI safety studies.